CHALMERS
UNIVERSITY OF TECHNOLOGY

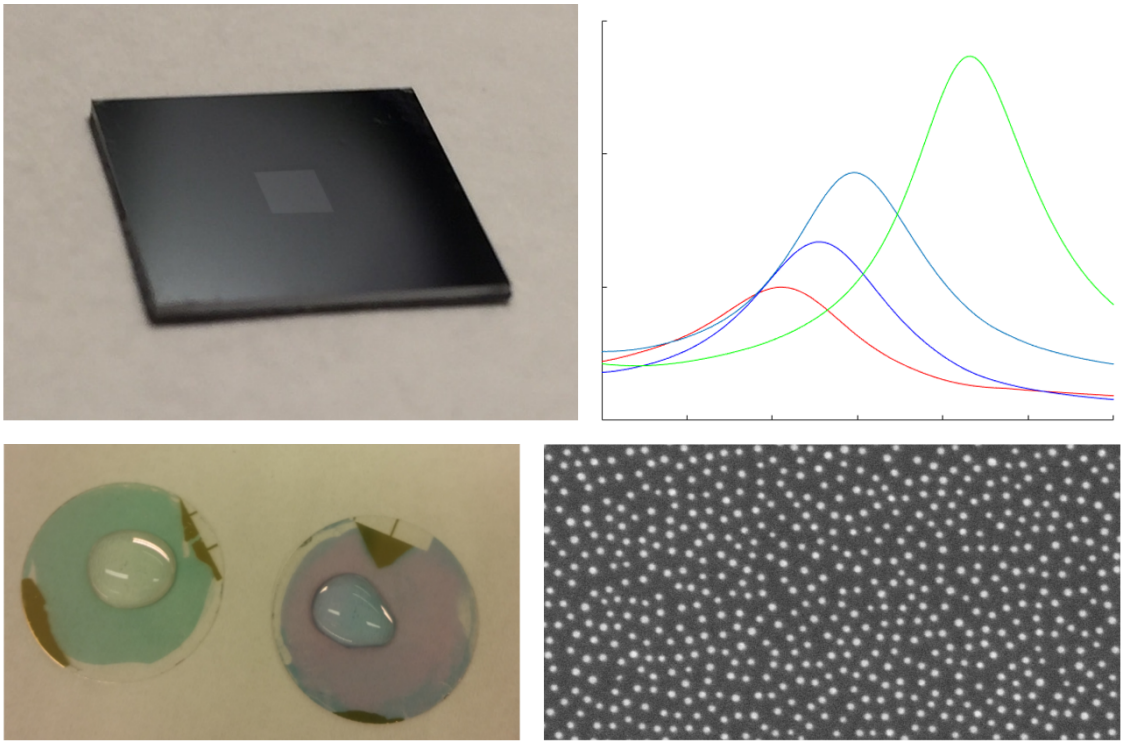

Integration of plasmonic nanostructures on waveguides

Master's thesis in Nanotechnology

Mattias Sjöberg

Department of Physics
CHALMERS UNIVERSITY OF TECHNOLOGY
Gothenburg, Sweden 2017

Master's thesis 2017

Integration of plasmonic nanostructures on waveguides

MATTIAS SJÖBERG

CHALMERS
UNIVERSITY OF TECHNOLOGY

Department of Physics
Division of Biological Physics
Chalmers University of Technology
Gothenburg, Sweden 2017

Integration of plasmonic nanostructures on waveguides
MATTIAS SJÖBERG

Supervisors: Björn Agnarsson and Mokhtar Mapar, Department of Physics
Examiner: Fredrik Höök, Department of Physics

Master's Thesis 2017
Department of Physics
Division of Biological Physics
Chalmers University of Technology
SE-412 96 Gothenburg
Telephone +46 31 772 1000

Cover: Up left, a photograph of the 1x1 cm^2 waveguide chip. Up right, the extinction spectra for gold nanodisks of different diameters. Down left, a photograph of droplets of water placed on gold nanodisk covered glass slides. Down right, an SEM image of gold nanodisks on a glass surface.

Printed by Chalmers Reproservice
Gothenburg, Sweden 2017

Integration of plasmonic nanostructures on waveguides
MATTIAS SJÖBERG
Department of Physics
Chalmers University of Technology

Abstract

Due to the limited sensitivity of many currently used single particle analyzation methods for the investigation of biological nanoparticles, such as exosomes and virions, many suffer from a bias towards the larger size ranges while sub 90 nm particles are potentially disregarded or less accurately analyzed. The division of Biological Physics at Chalmers has for the last couple of years been developing and testing a novel way of doing label-free biosensing. The method is based on waveguide evanescent-light microscopy using a silica core enveloped in a symmetric organic cladding with a refractive index matching that of water, which increases the sensitivity by minimizing the stray light background and allows for the label-free detection of single nanoparticles.
A protocol for the integration of plasmonic nanostructures on this waveguide was developed to investigate the potential of plasmon enhanced single-particle waveguide evanescent-light microscopy as a mean of unveiling the elusive nature of small biological nanoparticles. The well-established methods of colloidal and hole-mask colloidal lithography were used and adjusted to suit the specific requirements posed by the sensitive surface of the waveguide chip. A recipe for the integration is presented and a proof-of-concept experimental setup was used to analyze the potential of this platform as a biosensor. It was found that the coupling of single wavelength lasers and the subsequent observation of nanostructure intensity shifts is possible, but the desired high sensitivity and reliability requires the transition to very intensity stable and continuous light sources to allow for spectroscopy measurements to be carried out.

Keywords: Optical waveguide, localized surface plasmon resonance, gold nanodisk, colloidal lithography, biosensing, evanescent-light microscopy.

Acknowledgements

When working on this project for the past year I have had help from a number of people, without which this thesis would not exist. I herby thank you all. This has been a fun, interesting and educational year.

I thank **Björn Agnarsson** and **Mokhtar Mapar**, my supervisors, for guiding me through this project. For your help with the microscope, cleanroom work and our many discussions about my experiments and data.

I would also like to thank my examiner **Fredrik Höök** for insightful comments and for giving me the opportunity to work on this project.

A big thanks also to **Juliane Junesch**, for helping me a lot during the early phases of the project and for introducing me to the colloidal lithography method.

Thanks also to **Gustav Emilsson** for helping me with the spectrometry setup and to **Srdjan Acimovic** for our discussions about colloidal lithography.

I would also like to thank the entire **Biological Physics group** for being welcoming and friendly. I enjoy your company.

Thanks also to my family and friends, you mean a lot to me.

Soli Deo Gloria.

Mattias Sjöberg, Gothenburg, February 2017

Abbreviations

ACH	Aluminium chlorohydrate
CCD	Charge-coupled device
CL	Colloidal lithography
DI	Deionized
EBL	Electron-beam lithography
EV	Extracellular vesicle
HCL	Hole-mask colloidal lithography
HMDS	Hexamethyldisilazane
IBL	Ion beam lithography
IPA	Isopropanol
LSPR	Localized surface plasmon resonance
NA	NeutrAvidin
PBS	Phosphate-buffered saline
PDDA	Poly(diallyldimethylammonium chloride)
PDMS	Polydimethylsiloxane
PEG	Polyethylene glycol
PLL	Poly-L-lysine
PMMA	Poly(methyl methacrylate)
PVD	Physical vapor deposition
RIE	Reactive-ion etching
SAM	Self-assembled monolayer
SNR	Signal-to-noise ratio
SOG	Spin-On Glass
TIRF	Total internal reflection fluorescence
UV	Ultraviolet

Contents

List of Figures

1

Introduction

The field of nanotechnology has since its inception brought with it a constantly growing range of techniques for the manipulation of matter at the nanometer level. This has allowed for the harnessing of phenomena only accessible at these scales, opening up a wide range of novel technology and applications. One example of this is the field of biosensing where the possibilities of detecting and investigating biological nanoparticles have increased tremendously, leading to important progress in diagnostics, therapeutics and drug discovery [1, 2]. This introductory section of the thesis will provide some background to help the reader see the context in which the project is carried out.

1.1 Exosomes

Once considered artifacts of degenerated or dead cells with limited information content, extracellular vesicles (EVs) have in the past decades been identified as an important part of intercellular communication[3]. EVs are membrane enclosed biomolecular carriers in the hundred nm size range originating from various types of cells and are found in different bodily fluids such as blood, saliva and urine. [4, 5, 6]. Understanding the properties of EVs is an important endeavour not only because of their role in cell signaling but also for their potential use as biomarkers for diseases such as cancer and Alzheimer's disease[3, 7]. Studying the molecular composition, concentration and size distribution of this diverse set of biological entities at an individual level is a challenge because of their small size and because highly sensitive single molecule detection techniques are required. A number of techniques have been employed for studying the size distribution of EVs[8, 9], but many suffer from insufficient sensitivity for the lower size ranges or from the potential of damaging the vesicles or altering their properties.

Since the scattering of light for small hollow particles decreases with the radius to the fourth power[9], it is significantly more difficult to study the lower size ranges of EVs which can be at least as small as 30 nm in diameter[10]. Methods of EV analyzation depending on scattering could thus potentially be distorted as the smallest EVs are unintentionally ignored. A way of combating this issue is to make use of other properties of EVs than their scattering intensity, for example their refractive index.

1.2 Biosensing

A biosensor is a device used for the detection of an analyte through the combination of biological components and physiochemical technology[1]. It is usually described as consisting of three different components: a bio-recognition system, a signal transducer and a read out component. The recognition system is usually either based on or identical to a biomolecular analyte recognition system found in organisms. The selective properties of molecules such as single-stranded DNA, antibodies or antigens are used to interact with an analyte of interest and concentrate it on the transducer surface. The purpose of the signal transducer is to produce a measureable signal due to the presence of an analyte. It can take many forms but all share the property of detecting some kind of physical change upon analyte exposure. This could be scattering, as is the case for evanescent-light microscopy[9], weight for quartz crystal microbalances[11], conductivity for electrochemical biotransducers[12], or refractive index for plasmonic biosensors[13]. The read out component converts the transducer signal to processable data.The detection of target molecules have applications in a range of fields including diagnostics in healthcare and drug discovery.

Many biosensors used today would fit under the category of label-based technology[1]. In this family of techniques the analyte of interest is indirectly identified by being selectively associated with an element with an easily detectable property, such as fluorescence or radioactivity. The need of labeling the analyte has, however, several important drawbacks. The labeled molecules could be affected by the label in undesirable ways and have their properties changed, there could be issues with finding suitable labels for a certain kind of analyte and the labeling process can be time-consuming and expensive. *Label-free* detection techniques is therefore an increasingly important field of biosensing. These do, however, also involve a number of challenges such as the need of detecting very weak signals and the issue of distinguishing the analyte of interest from all other potentially signal-producing entities.

1.3 Plasmonics

Plasmonics is the study and application of the interaction of light and matter through optically excited collective oscillations of free electrons in a metal surface, called plasmons. A plasmon is a quantum of plasma oscillation, an electron density oscillation in conductive media, analoge to how a photon is a quantum of oscillation in the electromagnetic field. A *surface plasmon* is such an oscillation confined to the interface of materials with negative and positive permittivities[2]. For the excitation of a plasmon to occur in the visible part of the electromagnetic spectrum, the metal structure needs to be confined to the nanolevel in at least one dimension. If this is the case for all three spatial dimensions, the phenomenon of *localized surface plasmon resonance* (LSPR) is possible. One of the notable properties of LSPR is its highly enhancing effect on absorption and scattering of light at certain wavelengths. This produces colorful effects if the oscillation frequency coincides with the visible part of the electromagnetic spectrum.

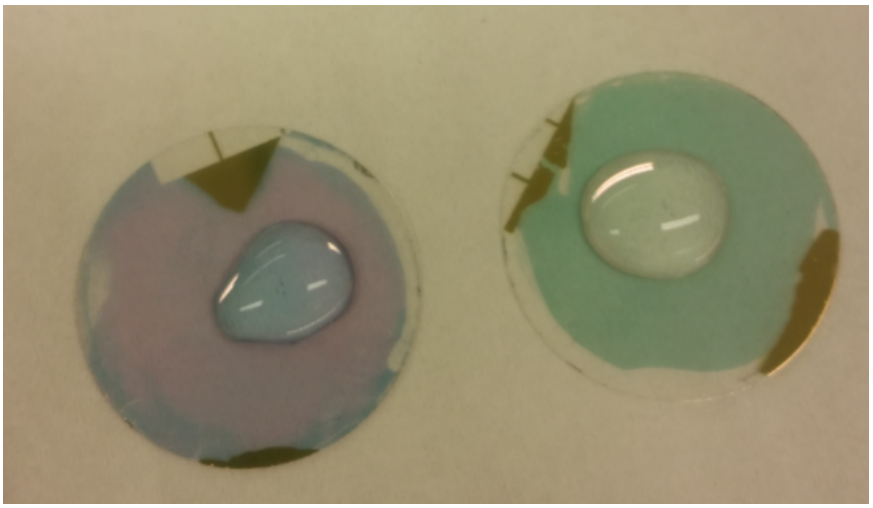

Figure 1.1: Glass slides covered with gold nanodisks. The LSPR is sensitive to the surrounding medium refractive index. The difference between air ($n \approx 1$) and water ($n \approx 1.33$) is clearly visible as a shift in color.

Since long before the theoretical understanding of the underlying principles emerged, the way metallic nanoparticles interacts with light and absorbs certain wavelengths due to LSPR have been used to produce colourful results. The stained glass used in church windows has for well over 1000 years been a prominent examples of this. The physics behind this effect was discovered by, among others, Michael Faraday[14] and Gustav Mie[15] over a century ago but it is not until recently, with the advent of nanotechnology, that plasmonic effects could be controlled and used for more than aesthetic purposes. Modern nanofabrication methods has brought with it the field of nanoplasmonics, where plasmonic effects are utilized for a wide range of applications including biosensing, photonics and photocatalysis[16, 17]. Biosensing using LSPR exploits the fact that the electromagnetic field for specific frequencies can be highly enhanced in the plasmonic nanostructure near field. This effect is sensitive to small changes in the refractive index of the surrounding medium. Figure 1.1 shows water drops placed on gold nanodisk coated glass slides, demonstrating the difference in absorbed wavelength depending on the refractive index of the environment. This makes possible the sensing of refractive index variations in the nanoscale volume surrounding a nanostructure. If carefully constructed and monitored, measurable effects on the far field appearance of the nanostructures can occur as single biological or chemical molecular entities enters the volume. This is the phenomenon used for nanoplasmonic biosensing. By selectively binding an analyte of interest to the surface of a plasmonic nanostructure and observing how the LSPR spectrum is changed, information can be extracted.

1.4 Aim

The main aim of this master's thesis is the development of a protocol for the fabrication of plasmonic nanostructures in the form of gold nanodisks on a waveguide chip,

the characterization of the optical properties of the device and to test its usability as a biosensor for detecting the binding of analytes (e.g vesicles). The waveguide chip is a device manufactured at the division of Biological Physics at Chalmers which is here further developed to include plasmonic components. The evanescent field from light guided in the waveguide will interact with the gold nanodisks creating an observable extinction band due to the LSPR phenomenon. Changes in the local environment of a disk surface will induce plasmonic shifts in the extinction spectrum. By choosing the size of the disks so that only the binding of a single vesicle per disk is possible and separating them enough to avoid optical coupling and signal overlap, each disk will act as an isolated sensor capable of detecting the binding of an individual bionanoparticle. This will make possible the simultaneous measurements of large amounts of vesicle binding events, providing the basis for statistical analysis.

2

Theory

2.1 Basic optics

2.1.1 Maxwell's equations

The interaction of light with matter of different shapes and materials can in classical theory be described by Maxwell's equations. These equations are the fundament on which electromagnetic field theory is built and are expressed as:

$$\nabla \cdot \boldsymbol{E} = \frac{1}{\epsilon}\rho \tag{2.1}$$

$$\nabla \cdot \boldsymbol{B} = 0 \tag{2.2}$$

$$\nabla \times \boldsymbol{E} = -\frac{\partial B}{\partial t} \tag{2.3}$$

$$\nabla \times \boldsymbol{B} = \mu \boldsymbol{J} + \mu\epsilon\frac{\partial \boldsymbol{E}}{\partial t} \tag{2.4}$$

Where $\boldsymbol{E}$ is the electric field, $\boldsymbol{B}$ the magnetic field, $\boldsymbol{J}$ the electric current density, ρ the free charge density, ϵ the permittivity and μ the permeability.
$\boldsymbol{J}$ is related to the electrical conductivity, σ, as

$$\boldsymbol{J} = \sigma \boldsymbol{E} \tag{2.5}$$

The permittivity and permeability are expressed as

$$\epsilon = \epsilon_0 \epsilon_r \tag{2.6}$$

$$\mu = \mu_0 \mu_r \tag{2.7}$$

where ϵ_0 and μ_0 are the vacuum permittivity and permeability while ϵ_r and μ_r are the relative permittivity and permeability.
By taking the curl of equation 2.3 and applying the vector identity $\nabla \times (\nabla \times \boldsymbol{E}) = \nabla(\nabla \cdot \boldsymbol{E}) - \nabla^2 \boldsymbol{E}$, a homogeneous wave equation is derived:

$$\nabla^2 \boldsymbol{E} = \epsilon\mu\frac{\partial^2 \boldsymbol{E}}{\partial t^2} \tag{2.8}$$

Assuming $\boldsymbol{E}$ to be an harmonic wave, $\boldsymbol{E}(\boldsymbol{r}, t) = \boldsymbol{E}(r)e^{i\omega t}$, gives us the Helmholtz equation:

$$\nabla^2 \boldsymbol{E} + \epsilon\mu\omega^2 \boldsymbol{E} = 0 \tag{2.9}$$

or

$$\nabla^2 \boldsymbol{E} + \epsilon_r\mu_r \frac{\omega^2}{c^2} \boldsymbol{E} = 0 \tag{2.10}$$

where $c = 1/\sqrt{\epsilon_0\mu_0}$ is the speed of light in vacuum and ω the angular frequency.

2.1.2 Optical properties of materials

In everyday life, the way a material interacts with light can be seen by its color which is caused by the frequency selective scattering and absorption of light by its electrons. This can be described in terms of the permittivity of the material $\epsilon(\omega)$, also called the dielectric function. This function describes the amount of attenuation an electric field undergoes in a material compared to the case in vacuum. In general, $\epsilon(\omega)$ is a complex function where the real part describes the amount of energy stored in the material. If Re$[\epsilon(\omega)] > 0$, the material is a dielectric, and if Re$[\epsilon(\omega)] < 0$, a metal. The imaginary part describes the lossiness of the material and is thus always positive. Lossiness is a property that describes dissipation of energy and is related the absorptive properties of the medium.

Another common way of discussing the optical properties of materials is in terms of the refractive index n, which is related the the dielectric function as $n^2 = \epsilon(\omega)$.
A dielectric material can usually, in the frequency intervals of interest, be assumed to be non-dispersive, i.e not dependent on the frequency; and non-lossy (meaning that Im$[\epsilon(\omega)]$=0 i.e the material is transparent). In this case the refractive index is simply $n = \sqrt{\epsilon}$.

In metals, where the real part of the dielectric function is negative, propagation is forbidden. Metals are thus reflective. This is true as long as the frequency of applied electromagnetic waves does not exceed the so called plasma frequency, ω_p, of the metal. Above this limit, the inertia of the electrons prevents their response to the oscillating field making the metal act as a dielectric. In this regime, transmission of electromagnetic waves is possible but is of limited importance here since it occurs far beyond the visible frequency interval, in the UV or X-ray ranges[1].

2.2 Plasmonics

2.2.1 Surface plasmons

Light affects a metal mainly by interacting with its free conduction electrons. One of these modes of interaction is the light induced collective oscillation of the free electron density in the metal, called a *plasmon*. The creation of a plasmon is only possible under certain conditions, for example when light is coupled to a metal-dielectric interface. Using clever matching of the light energy and momentum to the metal, a propagating wave of electron density variations can be induced, then called

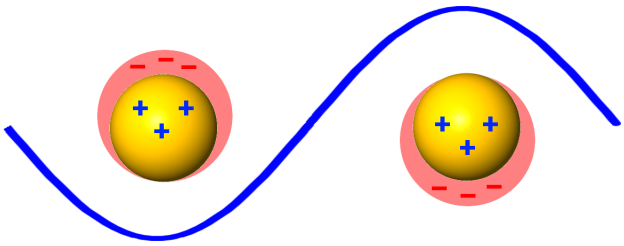

Figure 2.1: The delocalized electron cloud of a metal nanoparticle will interact with an incoming alternating electromagnetic field. The oscillation frequency depends on the particle size, shape, material and surrounding environment. An applied electric field of the same frequency will induce LSPR.

a *surface plasmon*. It can be compared to a water wave, a local variation confined to a surface. As the delocalized electrons are driven out of equilibrium there is a restoring electric field from the metal ions attracting the electrons against their direction of displacement. This is what drives the oscillation, not unlike a harmonic oscillator.

2.2.2 Localized surface plasmon resonance

If a metallic particle is small enough with respect the the wavelength of light, an induced free electron oscillation is confined in all directions, making it practically zero-dimensional. It will thus not propagate, as in the case above, but will instead just oscillate within the physical boundaries of the particle (see figure 2.1). The free electrons will move back and forth with a frequency highly dependent on the size, shape, material and local environment of the particle, since these parameters affects the strength and shape of the restoring electric field. If applying an external oscillating field of the same frequency, the electron oscillation will be driven into resonance, a phenomenon called *localized surface plasmon resonance* (LSPR). As the LSPR cannot propagate, it carries no momentum and is thus more easily induced than surface plasmons. Many metallic nanostructures will have surface plasmon resonances in the visible part of the electromagnetic spectrum, making possible the absorption and scattering of certain light intervals which creates colored samples. An LSPR sensor basically works by observing what wavelengths of light are absorbed by a metallic nanostructure and noting how this varies with changes in the local environment.

One of the most important characteristics of a nanoparticle for sensing applications is its extinction cross section, σ_{ext}. If a particle is illuminated with collimated light from a certain direction, σ_{ext} can be thought of as the area over which the particle affects the light by absorption and scattering. This area may be larger or smaller

than the geometrical cross section of the particle and could thus be seen as an analogue to the shadow of the particle. For objects that are large with respect to the wavelength of light ($a >> \lambda$), this area is equal to the geometrical cross section of the object but for smaller particles where this is not the case, this area is in general much smaller than the actual geometrical cross section of a particle. This is intuitively true since it would otherwise be impossible to see through air or water as the constituting molecules would shield all light passing through it. The extinction cross section, the "effective area" of an object can be derived to follow the relation [1]:

$$\sigma_{\text{ext}} = k_m \text{Im}(\alpha) \tag{2.11}$$

where α is the polarizability of the particle and k_m the wavevector in the surrounding medium.

Light interacting with a metal nanoparticle will either be scattered or absorbed [1]. The scattering cross section is expressed as:

$$\sigma_{\text{scat}} = \frac{k^4}{6\pi}|\alpha|^2 \tag{2.12}$$

The absorption cross section must then, due to the conservation of energy, be:

$$\sigma_{\text{abs}} = \sigma_{\text{ext}} - \sigma_{\text{scat}} \tag{2.13}$$

The electrodynamics of particles considerably smaller than the wavelength of light (with a radius $a << \lambda$) can be treated using the so called quasi-static approximation. In this range, applied fields are treated as static, with no temporal or spatial variation within the particle. An applied electric field $\boldsymbol{E}_0 = E_0 e^{-i\omega t}$ can thus be considered static by dropping the temporal oscillation part ($e^{-i\omega t}$). This reduces the complexity of calculations considerably by enabling electrostatics to be applied. This approximation can be used for particles of sizes in the 10-100 nm diameter range. For particles larger than this, the dynamics has to be considered, and for smaller particles, other effects becomes significant.

The extinction of a nanoparticle can be studied by observing the so called extinction spectrum, where the scattering and absorption of light is measured as a function of light illumination wavelength. An example of this can be seen in figure 2.2.
As is clear from equation 2.11, the polarizability α of a particle should be calculated to find the extinction cross-section. Finding α is the main challenge when working under the current assumptions and can in many cases be very difficult.

2.2.3 Spherical case

One of the simplest cases is that of a sphere in a dielectric environment, where both materials are homogenous and isotropic. By solving the Laplace equation under the right boundary conditions (see [18]), the following expression for the polarizability α is obtained:

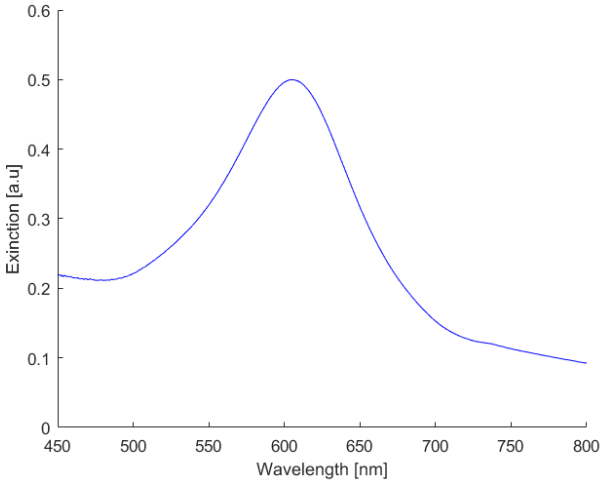

Figure 2.2: The extinction spectrum of a gold nanodisk. The extinction is a measurement of the amount of absorption and scattering of light which in this case is at a maximum at 605 nm. This is the LSPR wavelength.

$$\alpha = 4\pi a^3 \frac{\epsilon(\omega) - \epsilon_m}{\epsilon(\omega) + 2\epsilon_m} \tag{2.14}$$

where a is the radius of the sphere, $\epsilon(\omega)$ the dielectric function of the sphere and ϵ_m the dielectric function of the surrounding medium. ω is the angular frequency of the exciting radiation.
This gives us an expression for the induced dipole moment for the sphere:

$$\boldsymbol{P} = \epsilon_0 \epsilon_m \alpha \boldsymbol{E}_0 \tag{2.15}$$

By now combining equation 2.14 with equation 2.11, we get an expression for σ_{ext}[1, 19]:

$$\sigma_{ext}(\omega) = \frac{12\pi a^3 \omega \epsilon_m^{3/2}}{c} \frac{\mathrm{Im}(\epsilon(\omega))}{(\mathrm{Re}(\epsilon(\omega) + 2\epsilon_m))^2 + (\mathrm{Im}(\epsilon(\omega)))^2} \tag{2.16}$$

Using the relations $\lambda = 2\pi c/\omega$ and $\epsilon = n^2$, this can be expressed as:

$$\sigma_{ext}(\lambda) = \frac{24\pi^2 a^3 n_m^3}{\lambda} \frac{\mathrm{Im}(\epsilon(\lambda))}{(\mathrm{Re}(\epsilon(\lambda) + 2n_m^2))^2 + (\mathrm{Im}(\epsilon(\lambda)))^2} \tag{2.17}$$

As can be seen here, the extinction cross-section is a function of the wavelength of the incident light and has a maximum at the resonance wavelength corresponding to

$$(\mathrm{Re}(\epsilon(\lambda) + 2n_m^2))^2 + (\mathrm{Im}(\epsilon(\lambda)))^2 = 0 \tag{2.18}$$

It is possible to assume that $(\mathrm{Im}(\epsilon(\lambda)))^2$ is small for gold and silver nanoparticles [20], which simplifies the expression:

$$(\mathrm{Re}(\epsilon(\lambda) + 2n_m^2))^2 = 0 \tag{2.19}$$

This gives us the localized surface plasmon resonance, $\mathrm{Re}(\epsilon(\lambda)) = -2n_m^2$ or thus $\mathrm{Re}(\epsilon(\lambda)) = -2\epsilon_m$. When the wavelength of the incident light fulfills this relation, the interaction of the light and the spherical particle is maximized and the extinction cross section becomes significantly larger than otherwise.
Another important result can be seen by using the Drude model, where the free electrons in a metal are assumed to move classically in an environment of stationary ions[21], $\mathrm{Re}(\epsilon(\lambda))$ can then be expressed:

$$\mathrm{Re}(\epsilon(\lambda)) = 1 - \left(\frac{\lambda}{\lambda_p}\right)^2 \tag{2.20}$$

where λ_p is the plasma wavelength.

The condition in equation 2.19, combined with the expression in equation 2.20 gives that:

$$\lambda_{\mathrm{peak}} \propto \sqrt{2n_m^2 + 1} \tag{2.21}$$

where λ_{peak} is the wavelength of the LSPR, where the extinction cross-section has a maximum. This illustrates how a LSPR sensor works. A change in the surrounding medium refractive index n_m will give a detectable shift of the extinction spectrum peak position. Thus, if biological nanoparticles binds to a nanodisk in water, the local refractive index will increase as the $n = 1.33$ water is replaced by biological matter (which has a refractive index value $n \approx 1.5$ [22]), leading to a spectral shift. This is also conceptually understandable since a material with a higher refractive index (larger dielectric constant), will attenuate electric fields to a higher extent. The restoring force from the positive ion lattice acting on the oscillating negative electrons is thus weaker. In the analogy of the electron oscillations as an harmonic oscillator, the spring constant is reduced. The expression "the surrounding medium" refers for nanoparticles used in this thesis to a volume surrounding the nanoparticle extending a few dozens of nm from the surface[23, 24].

2.2.4 Spheroidal case

The nanodisks used in this thesis can be approximated as oblate spheroids, a geometric shape which also has a relatively simply expressed polarizability. An oblate spheroid is a special case of an ellipsoid, where two of the three semi-axes are equal (See figure 2.3).

An ellipsoid will have different polarizabilities along its different axes and will in general have polarizabilities α_j defined as[1]:

$$\alpha_j = \frac{4\pi R_1 R_2 R_3}{3} \frac{\epsilon(\omega) - \epsilon_m}{\epsilon_m + L_j(\epsilon(\omega) - \epsilon_m)} \tag{2.22}$$

where the index $j \in [1, 2, 3]$ defines the different axes, R_j is the semi-axes of the ellipsoid and L is the so called shape factor, a parameter defined by the shape of the ellipsoid. If $R_3 < R_1 = R_2$ applies, this describes the shape factor for an oblate

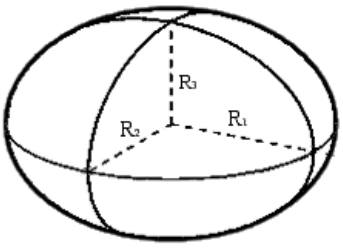

Figure 2.3: The special case of an ellipsoid where $R_3 < R_1 = R_2$, called an oblate spheroid.

spheroid.

The shape factor L is defined:

$$L_j = \frac{R_1 R_2 R_3}{2} \int_0^\infty ds \frac{1}{(s + R_j^2)\sqrt{(s + R_1^2)(s + R_2^2)(s + R_3^2)}} \tag{2.23}$$

When considering nanodisks instead of nanospheres, one of the more important differences is the reshifting of the LSPR. This shift is due to the fact that the restoring force from the positive metal ions is reduced along the elongated axis. This can be expressed in terms of the *aspect ratio* of the disks, the ratio between the diameter and thickness (R_1/R_3). A higher aspect ratio will result in a more redshifted main resonance position. Another effect of increasing the disk aspect ratio is that the LSPR peak width is reduced since the extinction is more concentrated to the resonance wavelength. A lower aspect ratio thus leads to a broadening of the peak.

The resonance condition for the ellipsoid, $\mathrm{Re}(\epsilon_m + L_j(\epsilon(\omega) - \epsilon_m)) = 0$, can be used to show that the extent of the shift in resonance peak position also depends on the nanodisk aspect ratio[25, 26]. A higher aspect ratio leads to a larger shift per refractive index unit, thus increasing the sensitivity. Other changes in particle shape will also affect the sensitivity. The interested reader is referred to[27].

Since the nanodisks used in this thesis are placed on a silica surface, only about half of the disk environment will be subjected to changes induced by bionanoparticle binding. In other words, no analytes can bind to the bottom of the disks. This leads to a decreased sensitivity, compared to plasmonic nanoparticles in solution[1]. When using nanodisk manufacturing techniques which creates disks in a randomly distributed pattern, the ensemble spectrum (the combined spectrum of a large amount of disks) will have a broader peak than that of a single disk due to the distribution of disk positions and sizes inherent to the manufacturing[28].

2.2.5 Coupling

In a system of nanostructures, the possibility of LSPR coupling exists. The coupling effects can be ordered into two categories, near-field and far-field. In near-field coupling, the electromagnetic fields of adjacent nanoparticles interact with each other, changing the LSPR characteristics. This effect occurs for particles with interparticle

distances in the order of 10 nm [29]. In far-field coupling, scattering from periodic structures creates diffractive effects that changes the LSPR.

2.3 Waveguide

When a propagating electromagnetic wave reaches an interface between two media of different refractive index, the phenomenon of total internal reflection can occur. If the wave travels from a higher to a lower refractive index material (e.g from glass to water or from water to air) and if the incident angle is above the so called critical angle, all the incoming energy is reflected[30]. This is, however, a somewhat simplified picture.

Since the solutions of Maxwell's equations must be continuous, there cannot be a point of discontinuity at the interface, where the field suddenly drops to zero. In fact, there is an exponentially decaying field on the other, forbidden, side of the interface called the evanescent field. This effect is analogous to the principle of quantum tunneling, where the wavefunction of a particle extends beyond a potential barrier. In this analogy the electromagnetic field is seen as the wavefunction of a photon. The exponential decay of the evanescent field means that any significant field strength is confined very close to the interface. The penetration depth of the evanescent field, defined as the distance from the surface where the amplitude has decreased to $1/e$ of its interfacial value, is often on the order of hundreds of nanometers.

One of the most common technological uses of total internal reflection is the optical fiber, in which light is perpetually reflected against the inner walls of the fiber, guiding it with small losses over large distances. A device like the optical fiber can in a more general sense be called a *waveguide*, a structure that can guide a wave with small losses by restricting its movements in some directions. The optical fibre is a one-dimensional waveguide, constricting the propagation of the light to one degree of freedom; but there are also two dimensional waveguides, where the wave is restricted to move in a plane (see figure 2.4). The light is guided through the core of the waveguide (purple) which is surrounded by cladding layers (blue), made of materials with a lower refractive index. This makes light coupled to the core confined through total internal reflection.

2.4 Propagation of light in a waveguide

To better analyze the wave propagation in a waveguide we go back to equation 2.10, the Helmholtz equation. Most optical media have a relative permeability, μ_r close to 1. If working under such an assumption and using that the refractive index $n = \sqrt{\epsilon_r}$ and the wavenumber $k = \omega/c$, we get:

$$\nabla^2 \boldsymbol{E} + k^2 n^2 \boldsymbol{E} = 0 \tag{2.24}$$

We can approximate the propagation of light in the waveguide as a plane wave in the x-direction (see figure 2.4 for definition of the coordinate system used in these

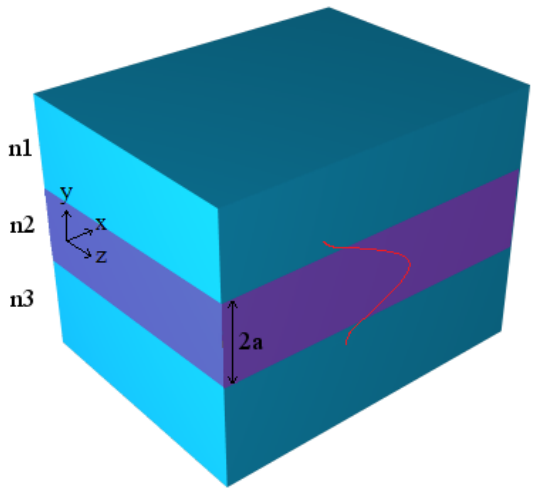

Figure 2.4: The structure of a two-dimensional waveguide. The purple core is embedded in the blue cladding layers. The defined coordinate system has the origo in the y-axis center of the core.

calculations, origo is placed in the middle of the core layer), i.e:

$$\boldsymbol{E}(\boldsymbol{r}) = \boldsymbol{E}(y,z)e^{-i\beta x} \tag{2.25}$$

where β is the wavenumber. Assuming a semi-infinite waveguide in the z-direction requires the independence of z for the solution to the electric field, thus:

$$\boldsymbol{E}(\boldsymbol{r}) = \boldsymbol{E}(y)e^{-i\beta x} \tag{2.26}$$

Combining equation 2.24 with equation 2.26 gives:

$$\frac{\partial^2 \boldsymbol{E}}{\partial x^2} + \frac{\partial^2 \boldsymbol{E}}{\partial y^2} + \frac{\partial^2 \boldsymbol{E}}{\partial z^2} + k^2 n^2 \boldsymbol{E} = 0 \tag{2.27}$$

which simplifies to:

$$\frac{\partial^2 \boldsymbol{E}}{\partial y^2} + (k^2 n^2 - \beta^2)\boldsymbol{E} = 0 \tag{2.28}$$

For a multi-layered system to act as a waveguide, the $(k^2n^2 - \beta^2)$-factor should be positive for the core and negative for the cladding layers. This is accomplished by using materials of different refractive index n (see figure 2.4). If chosen in such a way, equation 2.28 will have the solutions:

$$E = \begin{cases} A\cos(a\sqrt{k^2n_2^2 - \beta^2} - \phi)e^{-\sqrt{\beta^2 - k^2n_1^2}(x-a)} & y > a \\ A\cos(x\sqrt{k^2n_2^2 - \beta^2} - \phi) & -a < y < a \\ A\cos(a\sqrt{k^2n_2^2 - \beta^2} - \phi)e^{\sqrt{\beta^2 - k^2n_3^2}(x+a)} & y < -a \end{cases} \tag{2.29}$$

where the thickness of the core layer defined as $2a$; A is a constant that can be derived from the boundary condition of the electric field and the phase ϕ.

Here the exponentially decaying field in the cladding layers are evident, showing the confinement of the light to the core, where propagation occurs. If n_1 and n_3 are equal, i.e if the two cladding layers are made of the same material, the waveguide is considered symmetric.

2.4.1 Waveguide microscopy

Evanescent fields are often employed for biosensing purposes. Placing a biological sample on a surface under which total internal reflection of light occurs makes the illumination of just the thin region closest to the surface possible. This allows for the observation of the surface of samples, revealing features otherwise drained in the light of other sample parts. The excitation of fluorophores through the evanescent field of light totally reflected of a glass surface and the microscopical observation of their emission is called total internal reflection (TIRF) microscopy and is a commonly used method of studying biological samples[31].

A different approach is to use the evanescent field of a waveguide for biosensing. In this thesis a two-dimensional waveguide in the form of a sensor chip developed by Agnarsson et. al [9] is used. This symmetric planar waveguide consists of a 500 nm thick core of silica enveloped in a cladding layer of a fluorinated polymer, CYTOP. CYTOP is a material carefully chosen due to its rare property of having a refractive index (1.34) almost matching that of water (1.33). This index matching strongly reduces the stray light background present during a measurement since an unnecessary refractive index boundary is eliminated.

On each 1x1 cm^2 waveguide chip, there is a 2x2 mm^2 opening in the top CYTOP layer reaching all the way down to the core (see figure 2.5). In this area, the evanescent field of guided light in the core is available for usage to illuminate biological analytes. This has been used for, among other applications, the label-free characterization of lipid vesicles, investigation of protein binding and enzymatic (phospholipase A2) digestion of individual lipid vesicles and the observation of binding of Au nanoparticles by single vesicles[9].

There are a number of advantages with waveguide sensing compared to TIRF sensing. In TIRF, the illuminated area is more spatially limited and has a gaussian, non-uniform intensity distribution. TIRF also lacks the precise control of the evanescent field penetration depth offered by waveguide microscopy through the varying of the core layer thickness. Besides this, waveguide illumination places far fewer restrictions on the necessary optical setup compared to TIRF, which requires both an inverted microscope setup and a TIRF-compatible objective.

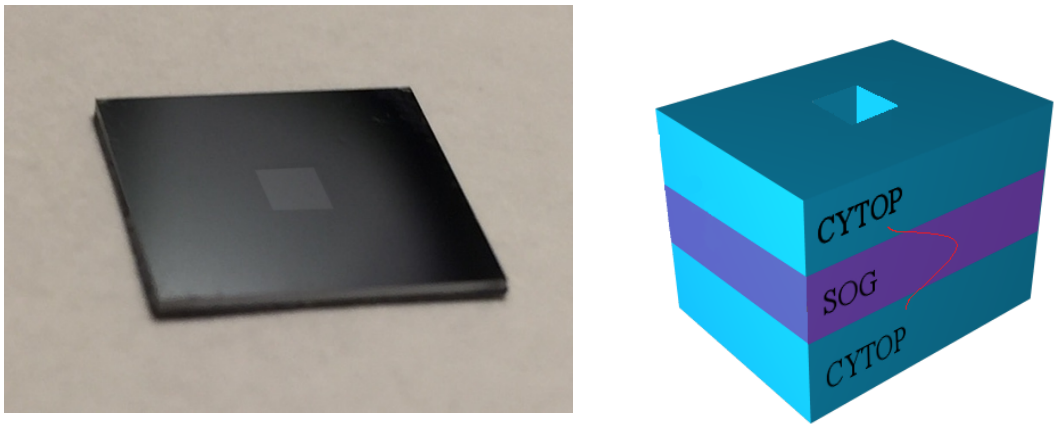

(a) **(b)**

Figure 2.5: a) Picture of a waveguide chip. b) Schematic of the waveguide structure with a well in the top cladding.

3
Methods

3.1 General principle

In this section, the methods used to develop and evaluate the manufacturing process are described. Before discussing the different aspects of the manufacturing process, the principle behind biosensing using this system is described, to put the methods into their proper context.

The system used for the detection of single biological nanoparticle binding events in this project, the plasmon enhanced single-particle waveguide evanescent-light microscopy, works in the following way. Laser light of two different wavelengths are coupled into a waveguide chip whose exposed core is coated with gold nanodisks. Upon illumination, LSPR will be excited in the gold disks which will shine like beacons due to the plasmon induced light scattering. The two laser wavelengths are tuned to the LSPR extinction spectrum to coincide with the slopes on the two sides of the LSPR peak (see figure 3.1). If an analyte is bound to a gold disk, the local refractive index will change which will shift the LSPR spectrum and lead to a simultaneous scattering intensity increase and decrease of the respective two laser wavelengths. Measuring these intensity shifts enables the detection of a binding event. A way of visualizing this in a clear way is to look at the quotient of the red and green scattered laser light. If the gold disks have been functionalized with molecules capable of selectively binding a certain analyte (the recognition system), the system can be used to identify the presence of this particular analyte in a solution. This analyte could for example be a subpopulation of EVs, containing a certain surface protein which can be exploited for identification by the recognition system.

To maximize the response in an experiment like this it is essential to have the laser wavelengths coincide with the maximum derivative parts of the LSPR extinction curve slopes. This enables a small shift in spectrum position to be translated to an as high scattering intensity shift as possible.
To make experiments like this possible, nanodisks placed on the waveguide core must fulfill a number of requirements.
The disks must:

- Be small enough to allow the binding of just a single vesicle per disk
- Adhere to the surface and not detach
- Be separated far enough to avoid optical coupling and signal overlap, which

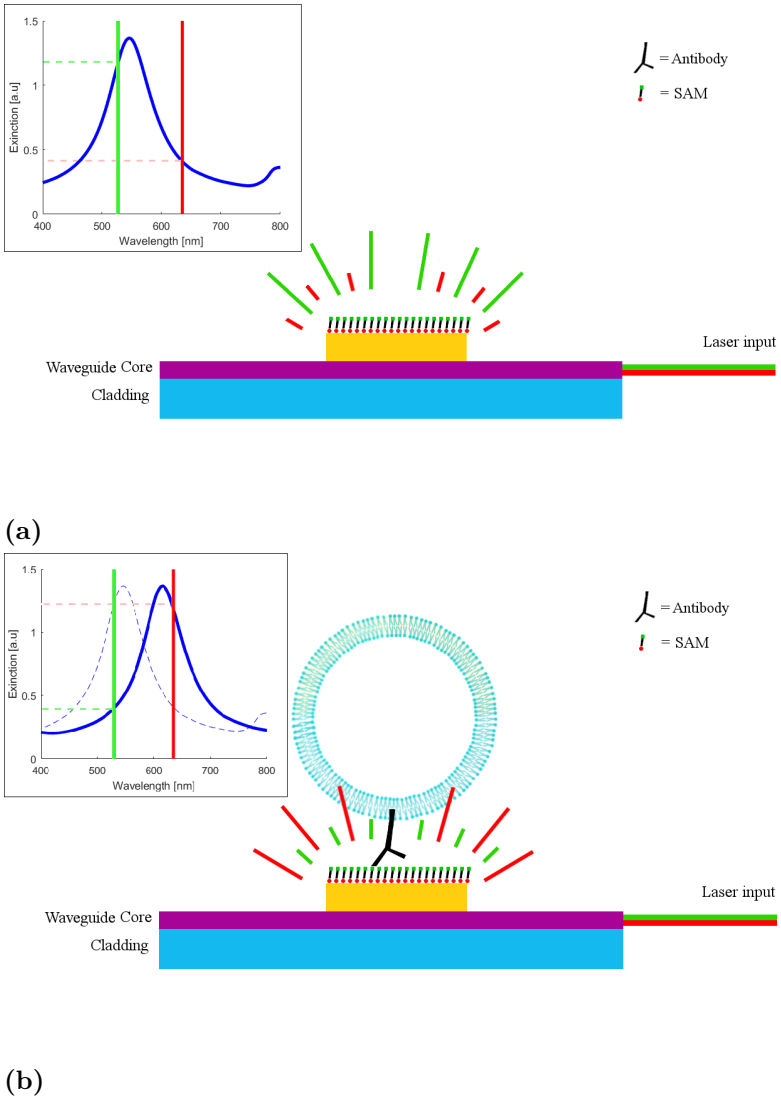

Figure 3.1: Overview of the basic working principles of transducing vesicle binding to a detectable signal with the optical microscope setup used in this project. The inserts show the optical extinction spectra of the gold nanodisks (blue) and the excitation laser wavelengths (green and red). In b) a vesicle is bound to the gold-disk which increases the local refractive index, leading to a redshift of the spectra. This places the LSPR frequency closer to the red laser wavelength which simultaneously increases the red and decreases the green scattering intensity. Observing these intensity shifts thus detects the binding.

would make the disk intensities interdependent or indistinguishable, respectively

The LSPR spectra of the disks must:

- Have sharp enough features to let a small resonance shift produce a detectable intensity shift
- Be tuned to correctly coincide with the used illumination laser wavelength

The tuning of LSPR properties for disks on a surface is mainly done through the variation of diameter, height and material.

3.2 Nanofabrication

To fabricate structures at the dimensions required for LSPR frequency to be located in the visible interval of the electromagnetic spectrum, matter needs to be manipulated at a very small level. Since the early days of micro and nano-fabrication a large range of different manufacturing techniques have been developed and a discussion of this field in general is beyond the scope of this thesis. This is a short introduction for the benefit of the unacquainted reader which if desiring more information is refered to[32, 33].

The commercial manufacturing of micro and nanostructures such as electronic components on computer chips, is dominated by a family of techniques called lithography. The general principle is that thin films of different materials are consecutively deposited on and partially removed from a surface. One of the most common methods is called photolithography and can be exemplified in the following way: A substrate is coated with a metal and is then covered with a photoresist, a material (usually a polymer) whose properties changes upon exposure to light. The surface is then covered with a mask with an engraved pattern that partially shadows the resist. After exposure to light of correct wavelength and intensity the mask pattern is transferred to the resist. The now partially changed properties of the photoresist is then used to selectively remove just one part of the pattern. This results in a resist pattern which partially covers and protects the underlying metal. The surface is then etched, a process which removes the exposed parts of the metal but leaves the protected parts unaffected. After removal of the remaining resist, the mask pattern has been transferred to the metal. Repeating this process makes possible the sequential construction of complex structures. The resolution of this method is limited by the diffraction limit set by the light wavelength used. Features smaller than around 200 nm can thus not be transferred using visible light. To beat the diffraction limit, current technologies use deep UV-radiation and immersion oils, decreasing this limit to approximately 50 nm. A way to drastically beat this limit is to use resists patterned by electron or ion beams instead, particles with significantly lower wavelengths than UV radiation, methods called Electron Beam Lithography (EBL) or Ion Beam Lithography (IBL), which allows for sub 10 nm resolutions to be achived[34].

There are two approaches for the manufacturing of nanostructures, top-down or bottom-up. In a top-down approach, structures are created by starting with a large

piece of a material and removing undesired parts until features on the nanoscale are produced. Building blocks are removed to fabricate the final structure. The lithographic methods described above are examples of this. A bottom-up approach instead starts with small building blocks and creates conditions for the blocks to self-assemble into desired patterns. Bottom-up fabrication is found in nature and covers how biological nanostructures are made. Single molecules assemble into complicated structures by themselves, without input from human intelligence. Top-down manufacturing is the approach currently dominating commercial nanofabrication as bottom-up currently gives significantly less control over the produced results. Being able to use bottom-up approaches for certain tasks is however highly desired because of its lower costs and potential higher throughput. Nature is able to assemble incredibly advanced structures, like plants and animals, using bottom-up so harvesting this potential for our use is highly sought after.

3.3 Nanofabrication methods used in this project

3.3.1 Sonication

Sonication or ultrasonic cleaning is the act of placing a sample in a liquid in which cavitation bubbles are induced through sound waves in the ultrasonic range. As the pressure in the liquid rapidly changes with the applied sound waves, bubbles are formed in the low pressure volumes which upon collapse releases a large amount of energy. This process can lead to the removal of a large range of contaminates from a surface[35].

3.3.2 Spin-coating

Spin-coating is a method for forming thin films of materials, e.g resists, on flat surfaces. A solution containing a resist is applied to the center of a substrate which is then spun at a high speed. The centrifugal force spreads the liquid over the substrate surface, making it form a thin film. The thickness of the film depends on the rotation speed, the liquid viscosity and the time. Thicknesses between 50 nm and 100 µm can be readily achieved by varying these parameters. A newly spun layer is often baked in an oven or on a hot-plate to evaporate the solvent, leaving behind a solid layer of resist.

3.3.3 Ion milling

One technique employed in this project for the removal of thin films is ion milling. This is a process where heavy ions are collided with a surface at high energy to inflict mechanical damage. To prevent the ions from causing chemical reactions at the surface, noble gases such as Argon is usually used. The Argon gas is injected into a vacuum pumped chamber and ionized by electron stripping due to an applied strong radio frequency electromagnetic field (usually 13.56 MHz). The newly formed Ar ions are then accelerated through a grid in the chamber wall by an applied potential between the grid and the sample holder. These high energy ions collide

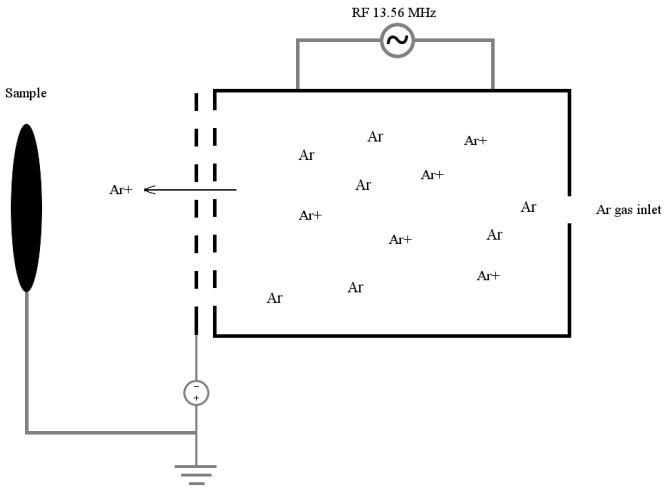

Figure 3.2: Illustration of the ion milling process. Ar+ ions are generated by applying a radio frequency electromagnetic field to Ar gas. The ions are then accelerated by an applied potential towards a sample whose surface is then milled.

with the sample surface, milling it and removing atoms at the surface. The ion flux and impact momentum is defined by the gas flux and applied potential difference between chamber and holder. This method is highly directional but can potentially cause unwanted damage to the underlying sample substrate. An illustration of the method can be seen in figure 3.2.
The Oxford Ionfab 300 Plasma etch-RIBE Ion beam System was used for Ar ion milling in this project.

3.3.4 Plasma treatments

Often called the fourth fundamental state of matter (besides solid, liquid and gas), plasma is a gas where electrons have been separated from the nuclei of its atoms and/or molecules. It is a mixture of free electrons and atomic, molecular, radical, ionic, excited and neutral species. For electrons to leave their atomic orbitals, a relatively large amount of energy is required meaning that naturally occurring plasma is often found in high temperature environments such as flames or lightnings. It is often used in lab environments for the cleaning, etching of surfaces or plasma enhanced chemical vapor deposition. A common way of generating plasma in the lab is to expose a gas to a high voltage radio frequency field (usually 13.56 MHz), accelerating the positively charged nuclei and negatively charged electrons in opposite directions with high enough energy to separate the two. Free electrons will accelerate and transfer energy to other, still bound, electrons leading to further ionization. Since the electrons are significantly lighter than the ions, they will accelerate more and hit the walls of the chamber and the surface while the heavier ions are relatively unaffected. An isolated surface in a chamber with grounded walls will build up a large charge which will in turn attract the ions. At the same time, the neutral plasma species, such as the radicals, will reach the wafer through diffusion

leading to the whole mixture of reactive species being present at the surface. This mixture now causes a range of processes, either direct sputtering of the surface or the removal of surface atoms through chemical reactions with the active species.

Depending on the purpose of the plasma treatment, different gases can be employed. If pure surface sputtering is desired, without chemical reactions, a noble gas such as Ar is used. This process works solely by the transfer of kinetic energy from the accelerated Ar ions to the surface.

Oxygen plasma works mainly by two types of interactions. Reactions occurring in oxygen plasma emits photons in so called vacuum ultraviolet range. These are energetically suitable for breaking most organic bonds (e.g., C-H, C-C, C=C, C-O, and C-N) and thus disassemble organic surface contaminants. Oxygen plasma also contains a range of oxygen species (O_2+, O_2-, O_3, O, O+, O-, and ionized ozone) which reacts with organic compounds to form high vapor pressure, low molecular weight species such as H2O, CO, CO_2. These will evaporate in the low pressure environment of the plasma chamber and be removed from the surface. Oxygen plasma treatment may lead to the oxidation of the surface. Besides cleaning the surface, oxygen plasma treatments are used to promote binding between a surface and liquid suspended molecules through the replacement of non-polar hydrogen bonds with oxygen bonds on the surface[36].

Hydrogen plasma works mainly through the process of chemical reduction instead of the oxidation processes in oxygen plasma. This is especially effective as a mean of removing undesirable oxides of a surface.

When a plasma treatment is used on a material which is removed relatively fast, such as PMMA, the treatment is called Reactive Ion Etching (RIE). The same treatment on a glass surface will, however, etch very little and is then used for surface cleaning. In this case the name ”plasma ashing” is more commonly used.

Two plasma treatment systems was used in this project, the Plasma Therm Batch-Top PE/RIE m/9 for RIE and cleaning during the disk manufacturing process and the Harrick Basic Plasma Cleaner for the surface activation before the SAM (self-assembled monolayer) formations of the chip surface.

3.3.5 Resistive thermal- and electron beam assisted- physical vapor deposition

Resistive thermal physical vapor deposition (PVD) is a method for depositing a thin layer of metal on a substrate. The material to be deposited, the source, is kept in a container of a low vapor pressure and high melting point such as tungsten which is heated through resistive heating. As the temperature increases, the source either starts sublimating or evaporating. The process is done in a vacuum chamber, pumped to operating pressures of $10^{-5} - 10^{-8}$ Torr to make the mean free path of the evaporated atoms much longer than the size of the chamber. This enables the

material to travel in straight lines and thus reaching a substrate placed in the line of sight of the source. The rate of deposition is monitored using a quartz crystal microbalance in the chamber.

Instead of resistive heating, the source can also be heated using an electron beam. Free electrons produced by a filament are then directed and accelerated by a magnetic field towards the source surface. As the kinetic energy of the electrons is lost upon absorption in the source, it is converted to other forms of energy, leading to the heating of the metal. The electron beam is usually swept across the source to produce a more uniform heating. This method has the advantage of directly heating the source and not transferring energy via the container which could otherwise potentially cause contaminations. In fact, the container is often actively cooled in electron beam PVD to avoid this problem. This also allows for evaporation and sublimation at higher temperatures which increases the deposition rate.
In this project, a Lesker PVD 225 electron beam PVD system and a Lesker nano36 resistive thermal PVD system were used.

3.3.6 Colloid-based lithography

In modern plasmonic research, the two most common bottom-up fabrication techniques are *colloidal lithography* (CL)[37] and *hole-mask colloidal lithography* (HCL)[38]. The advantages of these methods compared to top-down approaches capable of similar resolutions, such as Electron Beam Lithography, is their ability to cover large surfaces and their much lower manufacturing costs and lead times. They lack, however, the precision of EBL since control over the location of individual structures is not possible. The basic idea is that structures are defined by the immersing of a surface in a colloidal solution. Electrically charged colloids will attach to the surface and act as a mask in subsequent manufacturing process steps. The structures produced are thus the result of self-assembled patterns of colloids, controlled only at a large scale, average level. Though colloidal lithography techniques can cover large surfaces, this approach is highly limited in what structure shapes can be produced. However, with the use of angled evaporation and etching it is possible to extend the shapes from just circular disks to for example ellipsoids, cones, dimers and triangles[38, 39].

3.3.7 Self-assembly of colloids

Depositing a colloidal solution on a surface will, given proper conditions, lead to a self-assembled colloid pattern[40] which is commonly exploited as an etching mask in lithographic processes. A controlled adsorption of colloids can be achieved through electrostatic interactions between e.g negatively charged colloids and a positively charged polyelectrolyte layer deposited on a surface (e.g Aluminium Chlorohydrate or Polydiallyldimethylammonium chloride, ACH or PDDA). Attraction between the colloids and the surface will result in adsorption while repulsion between the similarly charged colloids prevents colloid aggregation, defining a inter-particle distance leading to a short range order. The colloid surface distribution is governed by a

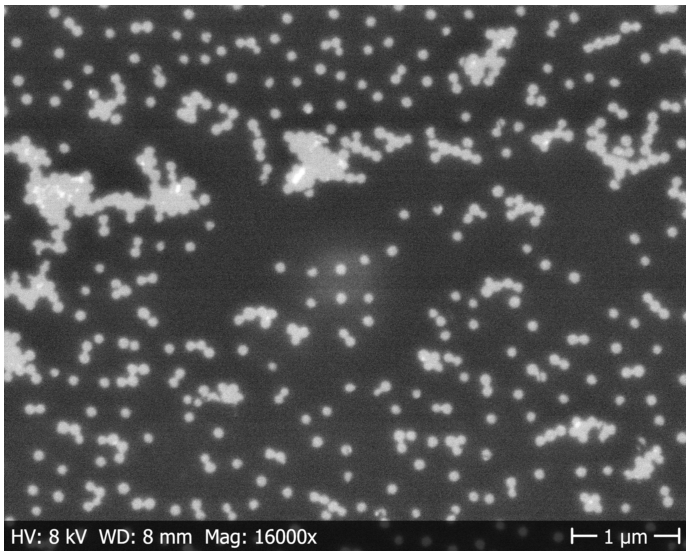

Figure 3.3: SEM image showing colloid aggregation as a result of insufficient N_2 blow-drying. The passive evaporation of water on the surface displaces the colloids and promotes aggregation.

multitude of parameters, including colloid concentration, surface charge, deposition time, solvent and most importantly the drying process. The drying procedure involves the rapid removal of excess solution through an intense flow of N_2 gas. If the solution is left to evaporate, the receding liquid front on the surface will move collides with it, altering the distribution and leading to colloid aggregation (see figure 3.3).

A typical colloid depsotion process consists of: i) Application of polyelectrolyte and subsequent N_2 blow drying to make the surface slightly positive. ii) Application of a colloidal solution and subsequent N_2 blow drying. The solutions are left on the surface for a determined amount of time to allow the colloid deposition to occur properly. When using a high colloid concentration the short range pattern is defined by the inter-particle distance defined by the particle-particle charge repulsion. This gives inter-particle distances far below the diffraction limit, so to observe individual particles optically, a highly reduced concentration has to be used where the colloid positions are instead random.

3.3.8 Fabrication of gold nanodisks

For the creation of gold nanodisks on the samples used in this project, two methods were employed, CL and HCL. The disks were made on two types of substrates, waveguide chips and borosilicate glass slides.The borosilicate slides act as control-substrates and allow optical properties of the nanostructures to be measured using a transmission spectrometer.

3.3.9 Colloidal lithography

In colloidal lithography, the self-assembly of colloids is used to define a mask on a metal coated clean surface. Before the electrolyte application, the surface is oxygen ashed to remove any organic residues. All metal not protected by the colloids is then removed by argon ion milling, leaving circular disks of metal on the underlying substrate. The removal of the now undesired colloids left on the disks is achieved using tape stripping, where a piece of tape is applied to the surface and subsequently removed after having adsorbed the colloids. The sample is then ashed in oxygen plasma to remove residues of polyelectrolyte from the surface. An illustration of the process steps is given in figure 3.4

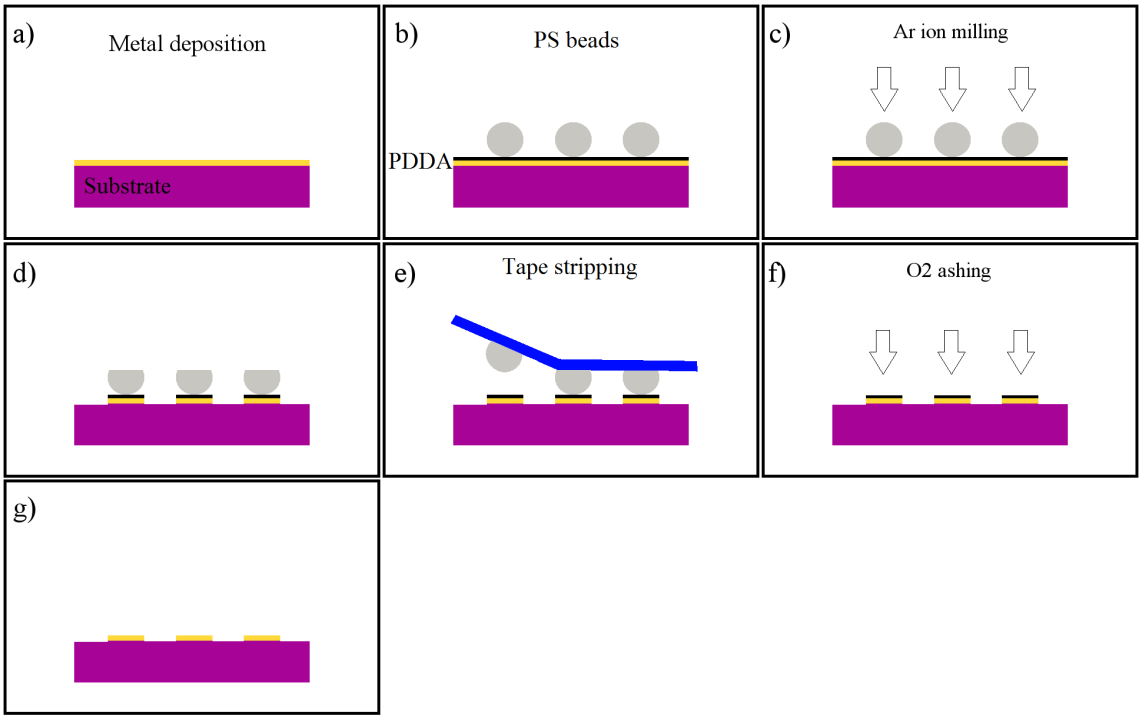

Figure 3.4: Overview of the steps in the CL process. a) Deposition of a metal thin film through PVD. b) Application of a polyelectrolyte such as PDDA and subsequent adsorption of polystyrene beads. c) Removal of the metal thin film not protected by the beads through Ar ion milling. e) Removal of the beads through tape stripping. f) Residue removal through oxygen plasma ashing.

3.3.10 Hole-mask colloidal lithography

In hole-mask colloidal lithography, a thin film of the polymer PMMA (Poly(methyl methacrylate)) is spin coated on a substrate to act as a sacrificial layer in a lift-off process. See figure 3.5 for an illustration of the process steps. The hydrophobicity of the PMMA is reduced through an oxygen plasma treatment after which colloids are deposited on its surface according to the above described process. A too hydrophobic surface risks being de-wetted during the polyelectrolyte and colloid deposition steps, potentially leading to an inhomogeneous colloid distribution. The hole mask is

then created through the PVD of a thin film of an oxygen-plasma resistant material such as Cr. After tape stripping of the colloids a mask has been created, protecting the underlying PMMA layer everywhere except on the previous location of the colloids, where there are now holes. Oxygen RIE is then used to remove PMMA in the exposed areas, resulting in wells through the sacrificial layer. A second PVD step is then used to create a film of metal on top of the mask and on the bottom of the wells. Finally, the PMMA layer is dissolved by placing the sample in acetone, leaving only the nanodisks behind on the surface.

Compared to the colloidal lithography method, HCL has the advantage of not etching the whole surface. It is preferable when working with sensitive substrates since it avoids the ion milling in the CL process. HCL does, however, have more steps and using it increases the complexity of the manufacturing. This brings with it more potential sources of problems, for example premature lift-off of the PMMA or inhomogeneous hole shapes.

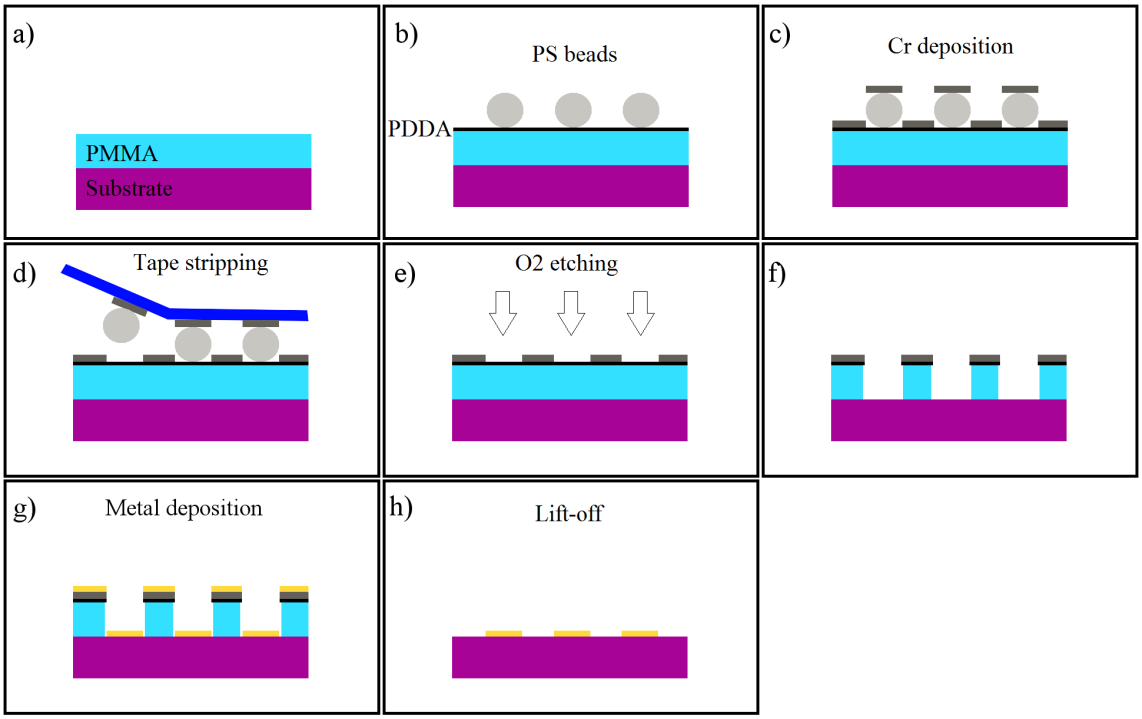

Figure 3.5: Overview of the steps in the HCL process. a) Application of PMMA through spin coating. b) Application of a polyelectrolyte such as PDDA and subsequent adsorption of polystyrene beads. c) Creation of a metal mask defined by the bead pattern through PVD of Cr. d) Removal of the beads through tape stripping. e) Oxygen plasma etching to create holes in the PMMA. g) Metal deposition through PVD. h) Lift-off by dissolution of the PMMA in acetone.

3.3.11 Fabrication of the waveguide chips

The waveguide chips used in this project consists of a 500 nm thick silica core (spin-on-glass, SOG, IC1-200 from Futurrex Inc.) enveloped in a 7 µm thick cladding

layer of CYTOP (CTX-809AP2 from AGC Chemicals, ASAHI Glass Co., LTD.) and was fabricated on a 4" Si wafer by sequential spin coating and baking of the different layers. 2x2 mm^2 wells in the top cladding layer were created through RIE. The surface was then covered with a thick layer of photoresist for protecting as the wafer was diced to 1x1 cm^2 chips. After the removal of the photoresist using the appropriate developer and rinsing in DI-water, the chips were dried using N_2 and stored in a clean room environment until the nanodisk deposition process was initiated.

3.4 Vesicles

One of the biological nanoparticles used as model system for the binding experiments in this thesis were lipid vesicles. A lipid is a amphiphilic, i.e part hydrophobic and part hydrophilic, molecule that under certain conditions self-assembles into nanoscopic spheres. In an aqueous environment, the hydrophobic parts are hidden by forming the inside of a so called lipid bilayer. The vesicles used in this project were prepared through extrusion of a lipid containing solution through a porous membrane[41]. While mainly consisting of POPC lipids (Polar Avanti lipids), the two kind of vesicles used here also contained Rhodamine labeled DHPE lipids and either anti-Biotin (BioLegend LEAF purified anti-Biotin 1D4-C5) or DSPE-PEG[2000]-Biotin lipids (Polar Avanti Lipids).

3.5 Surface chemistry

A key component in every biosensing technology is the link between the biological environment and the signal transducer. Self-assembled monolayers (SAMs), spontaneously formed ordered assemblies of surface components, are frequently used to modify surface properties and to introduce specificity in surface binding experiments. Molecules forming a SAM usually consist of three parts; the head which anchors the molecule to the surface, the backbone which stabilizes the monolayer through intermolecular van der Waals forces and the tail which constitutes the exposed part of the molecule. This exposed tail thus adds its properties to the surface, a process called functionalization[42, 43]. SAMs are used in this thesis for two purposes, the promotion of specific binding of analytes to gold nanodisks and the passivation of SOG surfaces to prevent unspecific binding.

Two methods of binding vesicles to gold nanodisks have been used in this thesis. Both exploit the, in biosciences, widely used binding properties of biotin. Biotin is a vitamin also known as B_7 which is part of a number of common binding systems. One of the strongest non-covalent interactions known in nature (with a dissociation constant of approximately 10^{-14} M) is the bond between biotin and the egg white protein avidin[44]. Avidin is a ≈68000 Da molecule with four binding sites for biotin. A protein similar to Avidin, NeutrAvidin (NA), is used in this thesis. It shares the benefits of a high association constant with biotin and the four binding sites but has been artificially deglycolized to highly reduce lectin binding to increase specificity.

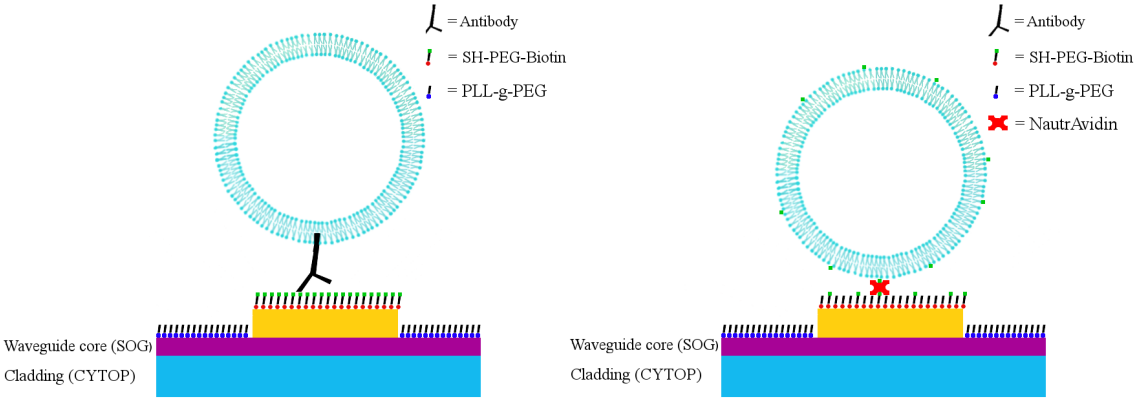

(a) **(b)**

Figure 3.6: The methods used for the binding of vesicles to gold disks. In a) a vesicle is bound directly to a disk through the interaction between an antibody and a biotinylated SAM. In b) a biotinylated vesicle is bound to a SAM coated disk through a NeutrAvidin intermediate.

The other biotin binding reaction used in this thesis is the binding between biotin and a biotin-antibody.

The utilization of these binding reactions requires the functionalization of the gold disks with biotin. This is achieved using the extensively studied strong bond between sulfur and gold in the form of a SAM system where alkanethiols bind to gold disks[42]. An alkanethiol-gold system has proved to be an excellent platform for SAM formation because of the inert nature of gold, the strong and highly specific thiol-gold interaction and the non-covalent interactions between the alkane chains, which enables monolayer formation. Alkanethiols exist with a wide variety of tail-groups providing the possibility of forming SAMs with different functions[45]. In this thesis, three different thiol compounds were used for the gold functionalization. The Polypure Thiol PEG biotin of 788 Da was used as the biotinylated part of the SAMs. The non-biotinylated thiol compounds used to control the surface biotin concentration was Polypure PEG Thiol (386.5 Da) or mPEG Thiol (356.5 Da). The compounds were diluted in 99.7% ethanol.

The binding of vesicles to a biotin presenting monolayer of alkanethiols on the gold disks is done by either anti-biotin functionalized vesicles which bind directly to the monolayer or by binding biotinylated vesicles using NeutrAvidin as a bridging-molecule (see figure 3.6). The anti-biotin approach (figure 3.6 a)) has the advantage of reduced complexity and involves fewer incubation steps but has the disadvantage of a lower binding affinity. The NA approach has the benefits of a very strong binding affinity and specificity but also needs an optimized concentration of surface biotin. It also places the analyte further from the gold disk, potentially leading to a decreased LSPR response.

Since each NeutrAvidin molecule has four biotin binding sites, a too high concentra-

tion of biotin at the gold surface will lead to the occupation of all sites before the vesicles are added. A mixture of thiol-PEG-biotin and thiol-PEG is thus required to provide an average of one biotin molecule per NA area. This concentration depends on the type of alkanethiol used, since longer PEG chains will shield a fraction of the biotin molecules.

When working with a low concentration of analytes, the localization of the binding events to the sites of detection (in this thesis: the gold nanodisks) can be critical for the outcome of a measurement[46]. This is achieved by the forming of a SAM with repellant properties on the areas surrounding the detection sites; the substrate is passivated.

For the passivation of the SOG surface between the gold nanodisks, poly-L-lysine (PLL) modified polyethylene glycol (PEG) was used, i.e PLL-g-PEG. PEG is a commonly used surface passivation molecule which spontaneously adheres to hydrophobic surfaces. While the mechanisms behind the surface passivation is not fully comprehended[47], the current understanding is that the PEG chains works like a water binding hydrogel brush whose passivating properties depend on their length, flexibility and density. The ethylene glycol chains form hydrogen bonds with the surrounding water which increases the surface hydrophilicity. The bound water acts as a steric barrier which prevents the analytes from absorbing to the underlying surface[48]. The PLL headgroup of the molecules allows surface modification to be performed in an aqueous environment and removes the constraint of having to work with hydrophobic surfaces.

The formation of a high quality SAM on a surface is a delicate process which requires a clean and correctly treated surface. Common treatments include hydrogen and oxygen plasma treatments, described above. In the final steps of the manufacturing protocols used in this thesis (see sections 4.1, 4.2), the chip surfaces is either rinsed in acetone and IPA or O_2 ashed. This treatment leaves the surfaces relatively free of contaminations. In addition to this, the chips are plasma ashed again immediately prior to the SAM functionalization.

The possibility of selectively functionalizing both gold and SiO_2 surfaces in the same system has previously been demonstrated by starting with the thiol chemistry, which modifies just the gold surfaces, and subsequently binding the PLL-functionalized molecules to the substrate[49]. The strategy used in this thesis is loosely based on that procedure and is as follows:

3.5.1 Plasma ashing

The pre-functionalization plasma treatment is done using either H_2 or O_2 plasma in either the Plasma Therm BatchTop PE/RIE m/95 at 40-50 W for 0.5-2 minutes; or the Harrick Basic Plasma Cleaner at 29.6 W for 3 minutes. With few exceptions, O_2 plasma gave a higher degree of specific vesicle binding to the Au disks.

3.5.2 Thiol chemistry

The chip is then incubated overnight in a thiol-PEG ethanolic solution. For the experiments using anti-biotin functionalized vesicles, 100 mol% poly-ethylene-glycol thiols with a terminal biotin group (SH-PEG-biotin, Polypure) was used, but for experiments instead using biotinylated vesicles and NA; a mixture of SH-PEG-biotin and SH-PEG was tested in different ratios. There is no consensus regarding the optimal ratio for these types of experiments[49, 50, 51], but one of the more common ones is to use 1 mol% SH-PEG-biotin and 99 mol% SH-PEG. To minimize contaminations from the atmosphere, the samples are then immediately placed in the thiol-PEG-biotin/thiol-PEG solution after the plasma treatment. After incubation the sample is sonicated for 15 seconds in ethanol to remove non-covalently bound thiols. A too long sonication can potentially remove the CYTOP cladding from the chip, rendering the sample useless. The sample is then rinsed in PBS to remove the ethanol and then dried in N_2

3.5.3 Functionalization of SOG

The sample is then incubated in a 50 µg/ml PLL(20)-g[3.5]- PEG(2) (SuSoS) PBS solution for at least three hours. The solution should be stirred a few times during this time to promote binding. After the incubation the sample is rinsed in PBS and kept wet until the next step.

3.5.4 NeutrAvidin

When used with biotinylated vesicles, the sample is incubated in a 200 µg/ml (300 nanomolar) NeutrAvidin PBS solution for 3 hours and then rinsed in PBS.

3.5.5 Vesicles

Vesicles are then added at 10 µg/ml while the surface of the sample is observed in the microscope setup.

3.6 Scanning electron microscopy (SEM)

An SEM is an electron microscope which creates images by scanning a beam of electrons over a surface and detecting the various signals originating from their interactions[52]. The so called *secondary electrons*, generated through the inelastic scattering of the beam electrons at the top few nanometers of the sample surface, provides information regarding the surface topography; while the *backscattered electrons*, elastically scattered from a volume extending further into the sample can reveal its atomic composition. Samples observable with SEM are limited to electrically conductive specimen since dielectric materials will charge over time when exposed to the electron beam. The observation of dielectric surfaces must therefore be done after the application of a conducting surface coating. Since the gold disks

imaged in this thesis are located on dielectric surfaces, they were coated with either 10 nm of Cr through PVD or the conductive polymer Espacer (Espacer 300Z, Showa Denko K.K.) through spin-coating. The JEOL JSM-6301F Scanning Electron Microscope was used during this thesis work.

3.7 Spectrometry

The spectral analysis of gold nanodisks coated glass slides was done using a B&WTek photodiode array spectrophotometer setup (see figure 3.7). This allows for the quick and straightforward acquisition of the extinction spectra without the use of a microscope or any advanced optics. The lack of a microscope has the drawback of not allowing for the observation of individual disks but instead just the average spectrum of a large number of disks, their so called ensemble spectrum. A sample is illuminated with a tungsten-halogen lamp using optical fibers and collimating lenses. The light transmitted through the sample is collected with an optical fiber and coupled to the spectrophotometer. Calculating the extinction spectra requires the measurement of the dark spectrum ($S_{dark}(\lambda)$) to account for false counts, and a reference spectrum (S_{ref} the signal without the sample).
The extinction is defined as[11]:

$$\epsilon(\lambda, t) = \log_{10} \frac{S_{\text{ref}}(\lambda)}{S(\lambda, t) - S_{\text{dark}}(\lambda)} \tag{3.1}$$

where $S(\lambda, t)$ is the measured spectrum of the sample at time t. To reduce shot noise, the intensity of the light source was increased to as high a value as possible without saturating the detector.

In experiments where the LSPR shift was tracked over time, the spectral data, $\epsilon(\lambda, t)$ was fitted to a high degree polynomial function whose centroid (center of mass) was tracked over time using Matlab and LabView software. Tracking the centroid instead of the peak gives a higher accuracy, since noise induced false peaks are disregarded[1]. Since there is no advanced optics that can focus on individual disks in this method, there needs to be a relatively high disk concentration to get a detectable extinction. Using a colloid concentration of 0.1wt% in the colloid solutions in the CL and HCL processes resulted in approximately 12 disks per μm^2 which proved to be enough. When measuring the spectra of disks immersed in liquid, two methods was used. These types of measurements are usually done using a flow cell, where the glass slide is contained in a tight, partially transparent chamber connected with small tubes for inlet and outlet of liquids. This is then connected to a pump which moves the liquids through the system. This was used when experiments requiring the ordered exchange of different solutions or the measuring of spectral changes over time. Since the use of a flow cell is relatively time consuming, fast snapshot measurements were done in another, simpler way. A PDMS well was manufactured, which could simply be attached to a sample, covered with a glass slide and filled with a liquid.

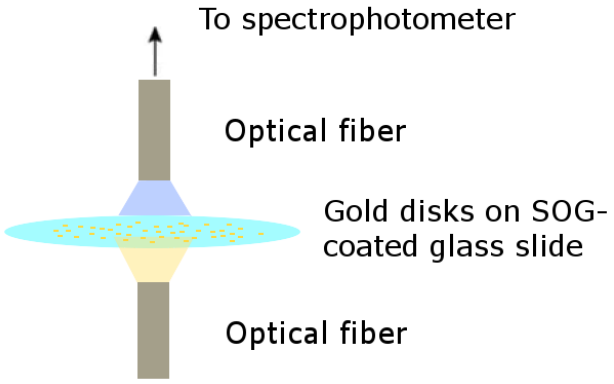

Figure 3.7: An illustration of the spectrophotometer setup used to observe the ensemble extinction spectra of gold disks on glass slides.

3.8 Experimental setup for binding measurements

To observe individual lipid vesicles binding to gold disks, the following experimental setup was used: Laser light is coupled to the waveguide chip core using an optical fiber mounted on a system of micrometer screw gauges which allows the positional fine tuning required for optimal coupling. The chip surface is observed with an Olympus BX61 microscope with a 100x water immersion objective and a ORCA-Flash4.0 V2 Digital CMOS camera (see figure 3.8 for overview of the setup). To observe two different wavelengths simultaneously, a Cairn OptoSplit II image splitter was used. This setup allows for the separation of different wavelength intervals into different channels by the use of a dichroic mirror and two filters. The dichroic mirror used in this setup reflects light with a wavelength <560 nm and transmits light of longer wavelength. The filters transmit 535 ± 50 nm and > 580 nm, respectively; which thus separates the 532 and 635 nm laser light used in this study. It also separates the excitation and emission wavelengths of rhodamine B, a fluorophore used to observe the vesicles.

3.9 Noise

When probing the spectral changes or intensity shifts of plasmonic nanostructures it is inevitable to have signal fluctuations, noise. This is due to a range of causes, some of which are discussed here.

3.9.1 Temperature

The refractive index, n, of a material is affected by its temperature. Water for instance, which is a large part of the environment in which the biosensing experiments in this project will occur, decreases with the temperature as:

$$-8 \cdot 10^{-5}\ \mathrm{K}^{-1} \tag{3.2}$$

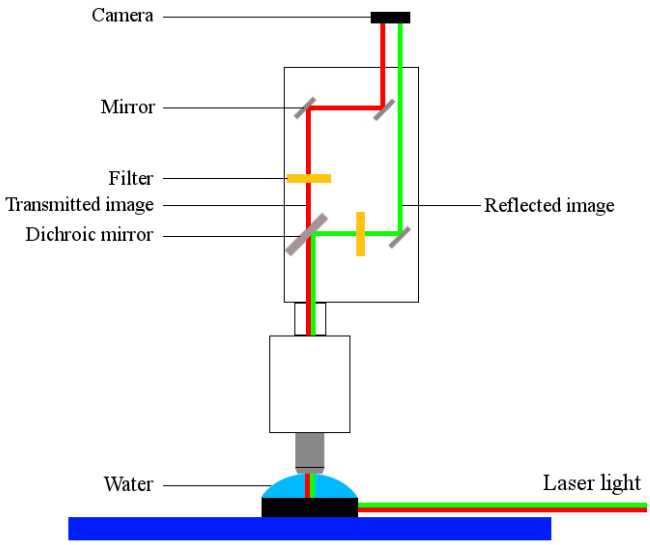

Figure 3.8: The experimental setup for the observation of the intensity shifts of nanodisks as biological nanoparticles are bound. A beamsplitter was used to separate the image into two channels of different wavelength intervals.

at room temperature. This is mainly due to the thermal expansion of water. Since intense light sources are used for exciting plasmons in the nanostructures, some temperature increase is expected over time. The refractive index of gold and silica also affected, with a frequency dependent effect[1].

3.9.2 Mechanical

Movement of the sample or of the sensing equipment can cause intensity fluctuations and great care should be taken when injecting fluids or handling the microscope during a measurement. Heat induced expansion of materials on the chips would also fit in this category. Small movements can affect the spectra, especially for single particle spectroscopy. It is necessary to have an as stationary sample as possible with respect to the microscope objective. To mitigate effects of vibrations in the building in which the experiments are done, the microscope is mounted on a halcyonics Micro 60 Active Vibration Isolation Desktop Unit.

3.9.3 Light source

All fluctuations in the input laser intensity will cause noise in the measurement system, especially in measurements where the whole spectrum is not continuously acquired. To mitigate this source of noise, the illumination intensity should be as stable as possible.

3.9.4 Shot noise

Shot noise originates from the quantized nature of light and is in many experimental setups the dominating source of noise. The number of photons traveling through an

area during a certain time period is a Poisson distributed random variable. Measuring the intensity is actually a measurement of the average photon flux. This gives an uncertainty that increases with intensity. However, a higher intensity still gives a better SNR since the signal increases faster than the shot noise. Maximizing the intensity at the detector to will thus maximize the SNR. Another approach for reducing shot noise is to average the intensity over several pixels[1].

4

Results and Discussion

The creation of gold nanodisks on waveguide chip surfaces was realized through the two different nanodisk fabrication methods described in section 3.2, hole-mask colloidal lithography and colloidal lithography. Several of the manufacturing steps in the methods were initially evaluated and tested through their use on transparent glass microscope coverslip substrates (Menzel Gläzer 25 mm diameter, 0.21 mm thick), which through their substantially lower costs and the enabling of the ensemble spectral analysis (see section 3.7) proved to be a suitable evaluation platform. The inherent requirement of sample transparency of the spectroscopy setup prevented the direct observation of gold disks on the waveguide this way. Since the process was to be transferred to the waveguide chips, HCL was initially chosen for the gold disk deposition to avoid the potentially damaging ion milling that CL requires. After the investigation and analyzation of the different manufacturing steps, the protocols described below were found to reliably produce nanodisks of adequate quality. The following sections will list these protocol steps with the finally established parameters for the two methods and then explain their implementation and evaluation.

4.1 Hole-mask colloidal lithography (HCL)

The following surface treatments will result in the creation of gold nanodisks on the SOG surface in the CYTOP well of a waveguide chip or on the surface of a glass slide. Refer back to figure 3.5 for an illustration of the steps.

- Sonication in acetone, IPA and DI-water (for glass slides only)
- N_2 blow drying
- Spin coating a 200 nm layer of PMMA A4 (3000 rpm, 60 s)
- Baking on a hotplate (90°C) for 10 minutes
- O_2 ashing for 5 seconds at 40 W, 250 mTorr
- PDDA solution application (0.2%) for 2 minutes, rinsing in DI-water and N_2 blow drying
- Colloid solution application ($3.33 \cdot 10^{-5}$ wt% or 0.1 wt%) for 80 s, rinsing in DI-water and N_2 blow drying
- PVD of 10 nm Cr
- Removal of colloids through tape stripping
- O_2 RIE at 40 W for 3 min
- Waiting at least 12 hours
- PVD of 1 nm Ti and 25 nm Au

- Lift-off by sonication in acetone until the metal covered PMMA layer is removed
- Rinsing in IPA and N_2 blow drying

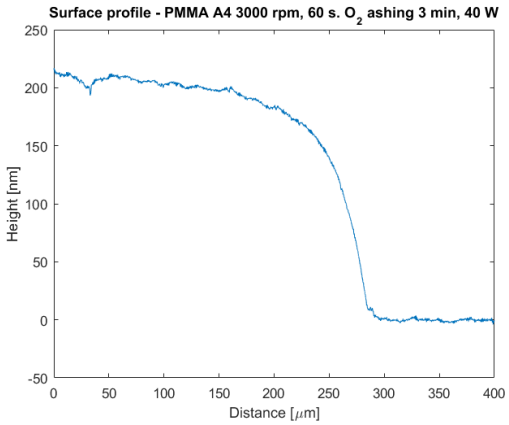

Figure 4.1: The surface profile of a glass slide covered in PMMA through spin coating (3000 rpm) which has been partially ashed in O2 plasma (40 W, 3 min). The PMMA layer thickness is approximately 200 nm.

4.1.1 Pre-PMMA application cleaning

The glass slide surfaces are cleaned by sonication (Elmasonic S) in acetone and IPA (for 3 minutes each) to remove potential contaminants and are then dried with N_2. Waveguide chips manufactured and kept in a cleanroom environment do generally not require any cleaning procedure before the later manufacturing steps but can be rinsed in acetone, IPA and DI-water (deionized water) if necessary. Sonication of the waveguide chips should preferably be avoided since it will risk detaching the top CYTOP layer from the SOG.

4.1.2 PMMA application

The first step of the HCL process is the spin coating of a polymethyl methacrylate A4 (950PMMA 4% diluted in anisole, MW=950000, MicroChem) lift-off layer. A spin speed of 3000 rpm for 60 s gives a layer thickness of approximately 200 nm [53]. To confirm this, a glass slide coated with PMMA using these parameters was partially covered with a protective glass slide and ashed for 3 minutes in O_2 plasma (at 40 W RF power, 250 mTorr operating pressure and 15 sccm O_2 flow). Figure 4.1 shows the surface profile of this sample which as expected revealed a step height of approximately 200 nm where the PMMA was etched away. Lowering the spin speed to 1500 rpm and increasing the time of ashing to 6 minutes instead gave a step height of 300 nm.

By consecutively O_2 ashing a PMMA A4 coated glass slide for 30 s and measuring the step height, the average etch rate for these settings and conditions was deter-

mined to 104.0 nm/min.

A potential problem of PMMA application on the waveguide through spin coating is its non-uniform surface structure. The 2×2 mm square well in the surface was hypothesized to potentially cause an uneven PMMA distribution and very gently sloped well walls. The surface inside the well is the intended location of the nanodisks and thus the area of most interest on the chip. It is therefore important that it contains a flat PMMA surface without significant inhomogeneities or slopes. Surface profilometry (with a Veeco Dektak D150 surface profiler) was used to investigate the PMMA distribution in the well after spin coating PMMA A4. The results can be seen in figure 4.2.

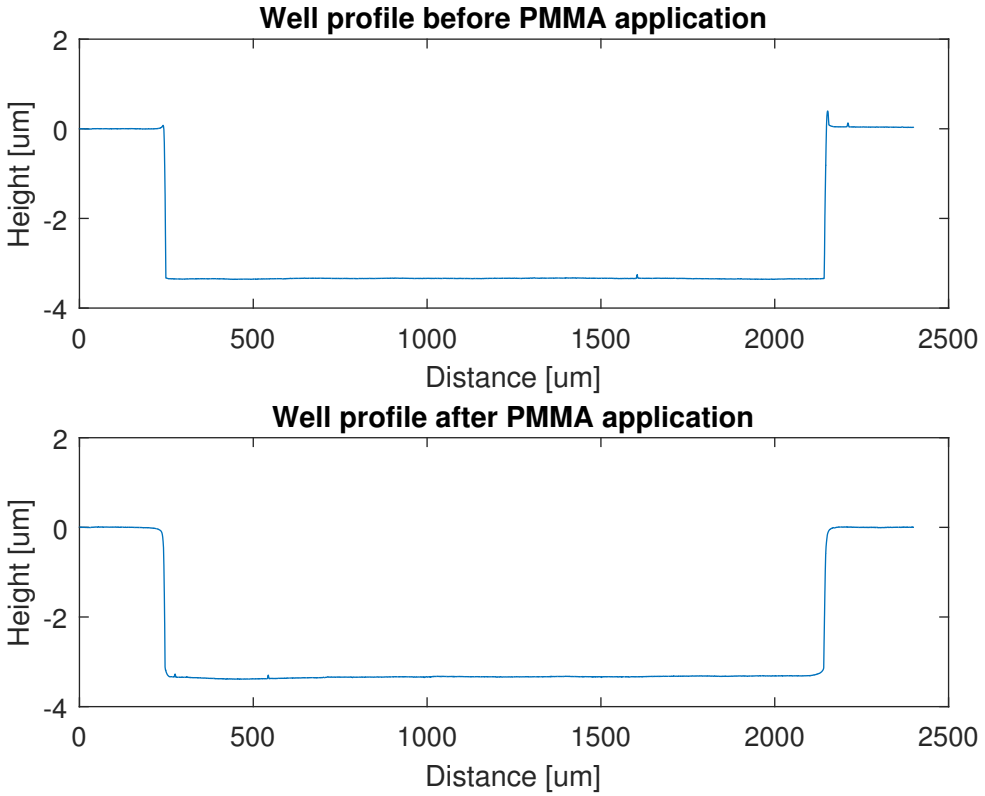

Figure 4.2: The surface profiles of the well in the waveguide chip before and after application of an approximately 200 nm layer of PMMA (spin coating, 3000 rpm for 60 seconds). The change in step height is about an order of magnitude lower than the applied layer thickness. This indicates that the PMMA is applied both to the silica layer at the bottom of the well and the CYTOP around it. The PMMA surface at the bottom of the well is relatively flat and is not a hindrance for the HCL process.

The depth of the well was approximately 11 nm smaller and the width changed less than 3 % after the application of the 200 nm PMMA layer. This indicates that the PMMA is applied to both the SOG and CYTOP and that nothing potentially process-disrupting happens at the walls. The peaks visible in the profile before

PMMA application at the edges of the well is significantly lower when scanning at a lower scanning speed. This suggests that the peaks are instrumental artifacts due to the preserved momentum of the profiler tip as is reaches the abrupt change of surface height. The artifacts disappear after the PMMA application, possibly since the slightly less steep edges provides a smoother transition for the tip.

After spin coating, the glass slides are baked on a hotplate to evaporate the anisole solvent and solidify the PMMA. The recommended baking temperature of 180 °C[53] exceeds the glass transition temperature of CYTOP at 108 °C [54]. To investigate the possibility of using a lower temperature with acceptable results, gold disks were deposited on two glass slides using identical processes except for the variation of baking temperature. No significant difference between samples using a baking temperature of 90 °C or 180 °C could be found. SEM images of these samples can be seen in figure 4.3.

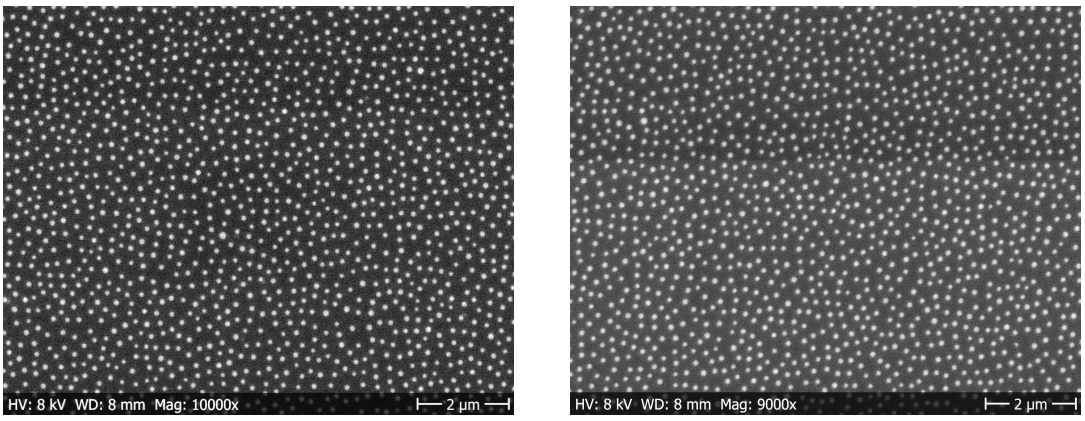

(a) 180 °C **(b)** 90 °C

Figure 4.3: Gold disks on glass slides created using the HCL process with a) 180 °C and b) 90 °C PMMA baking temperature. 100 nm colloids at a 0.1wt% concentration was used. The HCL process works for the lower PMMA baking temperature, which is necessary to avoid exceeding the 108 °C glass transition temperature of CYTOP when depositing disks on the waveguide.

4.1.3 Colloid deposition

An untreated PMMA surface is relatively hydrophobic which makes applied solutions easily drainable[36]. This effect is mitigated with a 5 s O_2 plasma treatment, which decreases the hydrophobicity through the addition of surface C-O and C=O groups which decreases the contact angle making the liquid cover less volatile.

After plasma treatment the surface is functionalized with polydiallyldimethylammonium chloride (PDDA, MW=200000-350000, 0.2% solution in deionized water) for at least 2 minutes, rinsed with DI-water and dried with a N_2 gun. The solution is applied through pipetting. This polyelectrolyte is positively charged and enables

the subsequent adhesion of the negatively charged colloids.

The next step is the application of a DI water solution containing negatively charged polystyrene (PS) colloids (Invitrogen). Colloids of different sizes were used throughout the project, ranging from 20-100 nm. Initially all samples underwent a heating procedure, where the substrate was placed under a flow of 100 °C ethylene glycole, after application of colloids to enhance colloid-surface adhesion, but experiments soon revealed this step to be unnecessary. In figure 4.4, an example of SEM images of two samples identically prepared except for the colloid heating can be seen. The inhomogeneous disk distribution and size in both samples are due to the 1 nm Cr adhesion layer, a subject treated below.

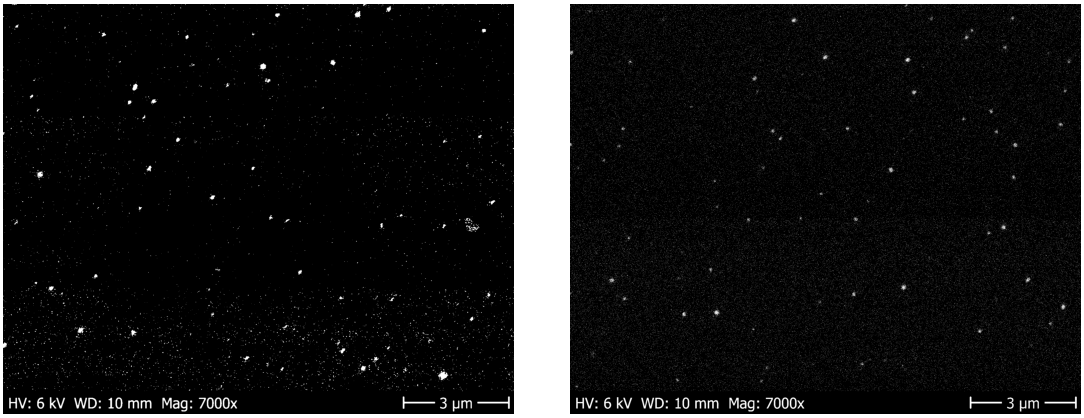

(a) **(b)**

Figure 4.4: Comparison between samples prepared with and without ethylene glycol heating after colloid deposition in the HCL protocol. a) Sample with 1 nm Cr and 25 nm Au where the PS colloids was heated with ethylene glycol after deposition. b) Sample with 1 nm Cr and 25 nm Au where the colloids was not heated after deposition. When analyzing the samples, there is no evident difference in colloid distribution.

The control of the colloid distribution is achieved through the varying of a number of parameters (see section 3.3.7). In this thesis, the colloid solution concentration and the time of solution application to the substrate was varied with the other parameters kept constant to find a set giving the desired mean inter-particle distance of 5 µm, a distance well beyond the diffraction limit set by the illuminating laser light. Differently prepared colloids can be seen in figure 4.5. Before observation with SEM, the surface was covered with a 20 nm Cr layer using PVD to increase to surface conductivity. The interparticle distances was analyzed using the image processing software ImageJ. The parameters finally chosen for the waveguide chips was 0.1wt%, diluted 3000 times ($3.33 \cdot 10^{-5}$ wt%). This concentration gives the inter-disk distance large enough to avoid coupling and image overlap due to diffraction while still giving enough disks per field-of-view to provide statistical analysis of binding. The field of view of the microscope setup used for the binding analysis allows for the simultaneous observation of a maximum of 298 particles if the mean interparticle

distance is 5 µm. To account for the expected inhomogeneous disk distribution, the number of disks should be considerably lower than this. Since the time did not have any clear effect, 80 seconds under static conditions was chosen as it proved convenient from a practical perspective in the lab.

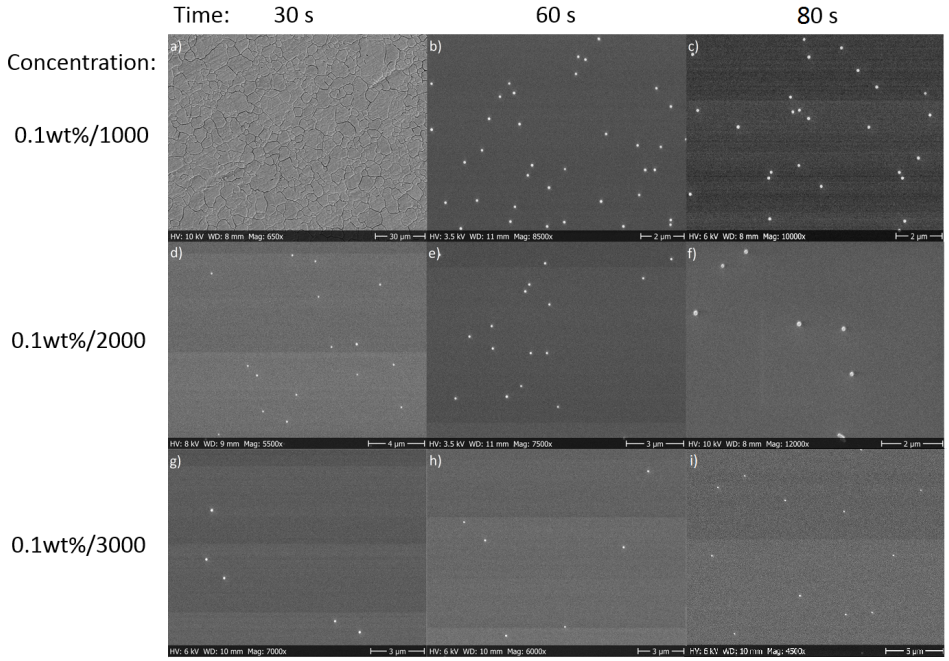

Figure 4.5: SEM images of glass slides covered with PS colloids according to the first steps of the HCL protocol, coated with a 20 nm layer of Cr. The x-axis shows the time the colloid solution is left on the substrate before rinsing with water and the y-axis shows the concentration of colloids in the solution. The distribution of colloids is clearly dependent on the concentration but no significant correlation with the time could be found. The first sample (top left) had no visible colloids and appeared damaged. Note the different scales in the images.

To get a observable ensemble signal for spectroscopic characterization of the nanodisks, a higher disk concentration is required. For this, a higher concentration of 0.1wt% was used, which is the commonly used concentration for the spectroscopic measurements in this thesis.

4.1.4 Mask creation

After the colloid application, a 10 nm Cr mask is deposited using the Lesker Nano 36 resistive thermal assisted PVD system (see figure 3.5 c)). This machine is configured specifically for Cr deposition and is cheaper and more accessible than the Lesker PVD 225 used for the Au and Ti deposition.

After the Cr deposition the Cr covered colloids are removed, leaving behind a hollow metal mask covering the PMMA (see figure 3.5 d)). This is accomplished using

two methods, tape stripping or the dragging of a spatula across the sample surface. When using tape stripping, a piece of cleanroom tape (Nitto SWT 10+R) is applied to the surface, pressed down by hand and slowly removed from one edge to the other. The tape consists of a blue transparent PVC film coated with a pressure sensitive acrylic-based adhesive, made to be free of contaminates and to have a moderate adhesion level. The tape has a tendency to not always adhere to the entire surface and will sometimes leave some small areas un-stripped. Because of this, tape is applied twice to make sure the whole surface is covered.

The last step in creating an evaporation mask is the reactive ion etching of the PMMA layer by O_2 plasma (see figure 3.5 e) and f)). The etching rate of PMMA A4 at 40 W had previously been determined to 104 nm/minute. A total etching time of 3 minutes was chosen, which gives 33% overetching to make sure that no contaminants remain at the surface. PMMA left on the surface will end up under the disks, potentially making them detach during the lift-off step.

During the initial testing phase of the protocol, a number of batches lacked nanodisks after completion of the fabrication protocol. It was discovered that the failed batches had in common that the O_2 plasma RIE was done the same day as the previous manufacturing steps. For some reason, waiting a number of hours, usually to the next day, is necessary for the process to work. One hypothesis is that since the PMMA is baked at half the recommended temperature of 180 °C, the PMMA is not completely dry afterwards. The etched holes in the still slightly viscous PMMA will thus get occluded over time and will not work as intended. Letting the samples sit in room temperature overnight makes the PMMA dry, and the etched holes permanent.

4.1.5 Disk deposition

The next step is to deposit gold to the exposed substrate (see figure 3.5 g)). Since gold generally adheres poorly to silica substrates, a nanometer-scale layer of a second metal such as Cr or Ti is often employed as an adhesion promoter[2]. Because of the highly optically absorptive properties of these metals, this layer is likely to damp the LSPR and thus reduce sensitivity of any nanoplasmonic biosensor. It is therefore important to minimize the thickness of the adhesion layer. Both Cr and Ti was tested. Cr has the advantage over Ti that it is compatible with the RCA1 cleaning protocol[55], commonly used before SAM formation but since RCA1 is likely to damage the CYTOP on the waveguides, it is not used in this project.

Figure 4.6 shows SEM images of samples prepared with 1 nm and 3 nm Cr adhesion layer thicknesses. Examining the samples reveals a considerably higher uniformity in size and shape for the 3 nm adhesion layer sample. Increasing the adhesion layer thickness does, however, increase the LSPR dampening effect. In figure 4.7 a similar sample can be seen, where 1 nm Ti was used instead. Multiple tests showed that this gives a uniformity comparable to the 3 nm Cr layer.

To investigate how the LSPR is affected by the different disk geometries, the extinc-

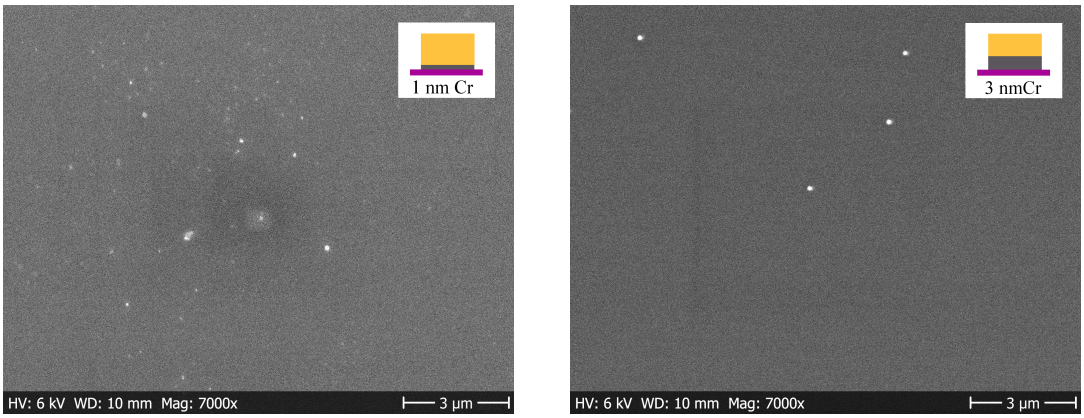

(a) **(b)**

Figure 4.6: 100 nm diameter nanodisks on glass slides prepared according to the HCL protocol consisting of a) 1 nm Cr and 25 nm Au and b) 3 nm Cr and 25 nm Au.

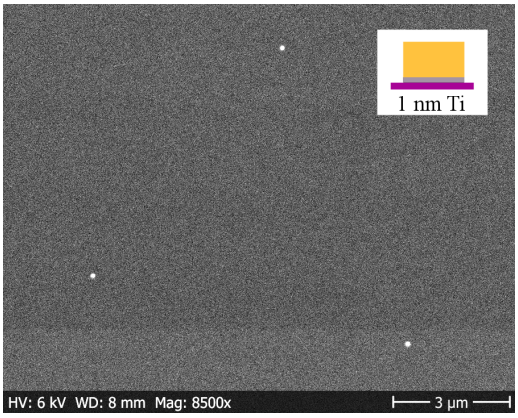

Figure 4.7: 100 nm diameter nanodisks on a glass slide prepared according to the HCL protocol consisting of 1 nm Ti and 25 nm Au.

tion spectra was measured using the spectrometry setup discussed in section 3.7. Figure 4.8 a) shows the dampening effect of a thick Cr adhesion layer and b) shows the broadening effect of increasing the disk height. Since steep slopes is a desired spectral property, disks should have sharp and high peaks. Ti is thus prefered over Cr since it damps the LSPR less and makes possible the use of a thinner adhesion layer. The gold layer should also be kept thin, to reduce the peak width. Figure 4.9 shows the spectra for disks of 41 nm and 63 nm diameters, taken in an air and water environment. This demonstrates the LSPR dependence on refractive index as the peak is redshifted when the sample is placed in water.

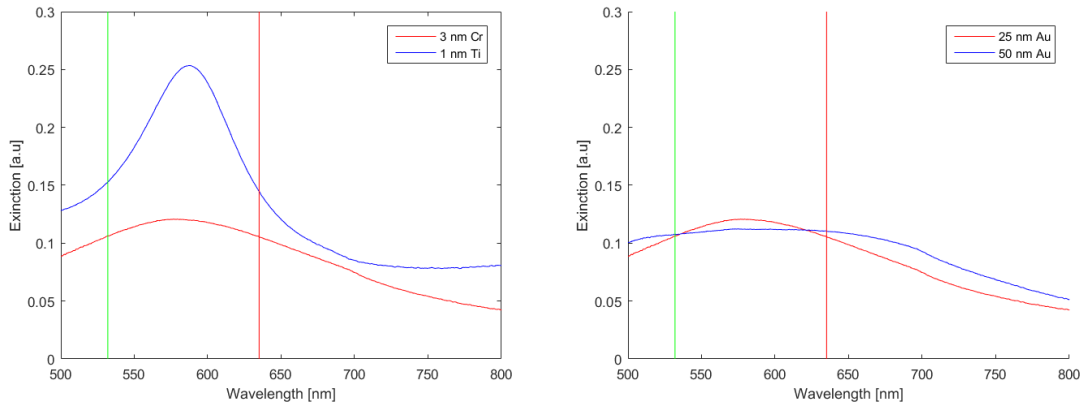

(a) **(b)**

Figure 4.8: a) Comparison of the resonance peak for 25 nm Au disks with different adhesion layers. The dampening effect of a 3 nm Cr layer compared to a 1 nm Ti layer can clearly be seen. The horizontal lines represents the wavelengths of the available lasers in the experimental setup for measuring binding events. b) Extinction spectra of glass slides covered with 63 nm diameter nanodisks of 3 nm Cr and 25 nm or 50 nm Au. The broadening effect of the resonance peak is evident when comparing the two spectra.

4.1.6 Lift-off

By dissolving the PMMA layer in acetone, all materials deposited on top of this lift-off layer are removed from the chip (see figure 3.5 h)). The lift-off process for samples created using the high concentration of colloids (0.1wt%) worked without complications. As the chip is submerged in acetone and the metal layer is visibly removed within a minute. When using the highly diluted colloid solutions, used for the waveguides, the lift-off using this method had a relatively high failure rate. A possible explanation for this is that the lower amount of holes in the layer reduces the exposed PMMA surface area significantly which either slows down the dissolution process or dissolves the PMMA while leaving the covering metal layer intact and adhering to the underlying substrate. To combat this issue, the thickness of the PMMA layer was increased to 300 nm by decreasing the PMMA spin-coating speed to 1500 rpm. Furthermore the samples were sonicated in acetone during the lift-off, then rinsed in IPA to remove possible contaminants and dried with N_2.

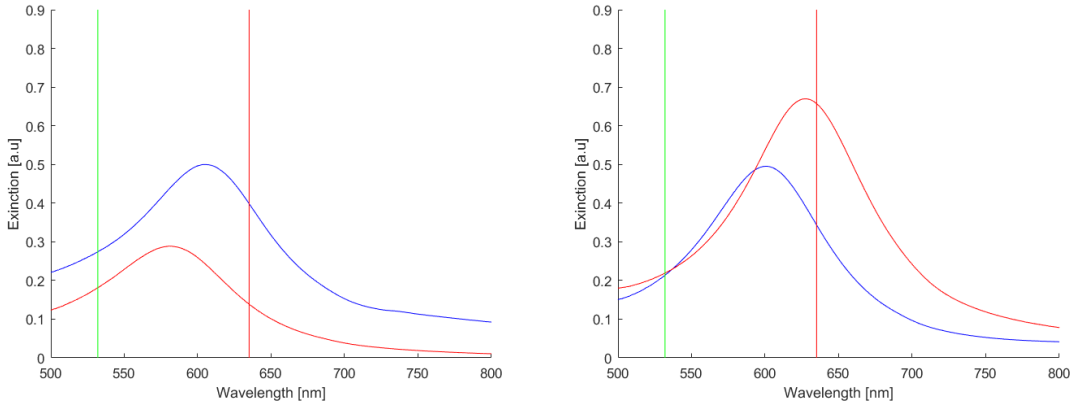

(a) **(b)**

Figure 4.9: a) Extinction spectra of glass slides covered with 41 nm diameter nanodisks of 1 nm Ti and 25 nm with the CL protocol in air and water. b) Extinction spectra of glass slides covered with 63 nm diameter nanodisks of 1 nm Ti and 25 nm with the CL protocol in air and water.

4.2 Colloidal lithography (CL)

Since the substrate material affects the LSPR wavelength, gold nanodisks immediately deposited on borosilicate glass slides will not give a representative spectrum of the disks as they appear when placed on the waveguide core layer (SOG). To better model the disk spectrum, glass slides with SOG were prepared before the nanodisk application.

After sonicating glass slides in acetone and IPA and blow drying with N_2, SOG was applied through spin coating (500 rpm for 5 sec 1000 rpm for 60 sec with 2500 rpm/s acceleration for the first ramp). The samples were then baked for 24 hours at 120°C in a vacuum oven.

During the tape stripping step in the HCL protocol, samples made on SOG-covered glass slides lost parts of the PMMA layer as it stuck to the tape and was detached from the chip. The removal of the PMMA-Cr mask before the Ti and Au deposition ruins the manufacturing process since no disks can then be created. One possible explanation for this is that the different surface properties of SOG, compared to borosilicate glass slides, makes the PMMA adhesion worse. This problem with the HCL process was, however, only present when used for disk creation on SOG coated glass slides and was not an issue for the SOG in the waveguide chip wells. It is not clear why this is the case, but it is possible that it is due to the SOG surface properties changing in the chip manufacturing process. One way of avoiding the problem is to remove the colloids using a spatula instead of with tape stripping. By carefully dragging a soft plastic spatula over the surface the colloids are removed. This worked with somewhat dissatisfactory results. The colloids were removed but a number of scratches in the Cr mask were always present afterwards (see figure 4.10). Unsuccessful attempts were made to promote adhesion by the application of

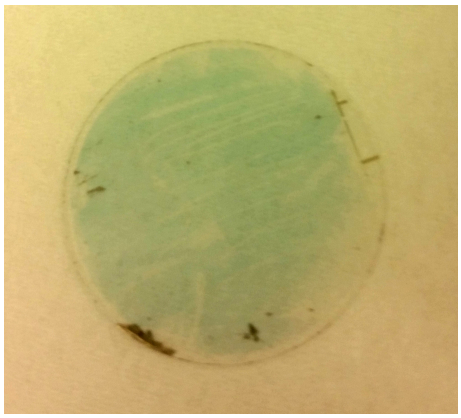

Figure 4.10: Picture of a glass slide covered with gold disks where the colloids were removed with the use of a spatula during the HCL process. The scratches due to this treatment are clearly visible here.

a HMDS layer before the PMMA spin coating. HMDS, hexamethyldisilazane, is a widely used adhesion promoter in nanofabrication. It is applied in gaseous form to heated substrate. The HMDS was applied using a Vapor Prime QS V 200 BM.
The inadequate results of these attempts at using HCL on SOG-coated glass slides made it necessary to instead use CL for disk deposition. In this method, the use of PMMA is avoided.

The CL protocol is presented below, with explanations of the steps distinct from the HCL protocol following. Refer back to figure 3.4 for an illustration of the steps.

- Sonication in acetone, IPA (Isopropanol) and DI-water. (for glass slides)
- N_2 blow drying
- PVD of 1 nm Ti and 25 nm Au
- O_2 ashing for 5 seconds at 40 W
- Covering the surface with PDDA solution (0.2%) for 2 minutes, rinsing in DI-water and drying with N_2
- Covering the surface with colloid solution ($3.33 \cdot 10^{-5}$ wt% or 0.1 wt%) for 80 s, rinsing in DI-water and drying with N_2
- Ar ion milling (30 mA beam current, 500 V beam voltage, 339 V acc. voltage, 30 mA neutr. current)
- Removal of colloids through tape stripping
- O_2 ashing at 40 W for 2 minutes

4.2.1 Ion milling

The milling of the metal layer surrounding the colloids (see figure 3.4) was done using the Oxford Ionfab 300 plasma etch-RIBE ion beam system with 30 mA beam current, 500 V beam voltage, 339 V acceleration voltage and 30 mA neutralizer current. Since this process is quite damaging to the substrate, excessive overetching is undesired. The etching time was calibrated by etching a glass slide coated with 1 nm Ti and 25 nm Au for consecutive 10 s intervals and examining the surface

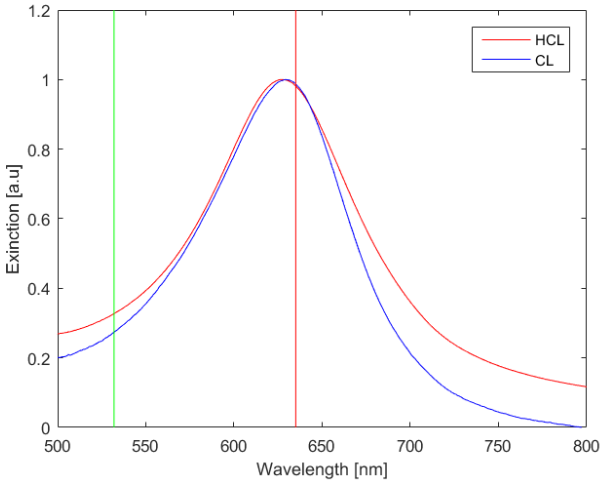

Figure 4.11: Optical extinction spectra for disks of prepared with hole-mask colloidal lithography and colloidal lithography. The disks are 63 nm diameter and made of 1 nm Ti and 25 nm Au. The differences in centroid position is 2.2 nm.

between each repeat. The finally chosen etching time was 85 seconds.

A potential complication of the ion milling process is the fact that as the gold on the surface is milled, so are the colloids. The spherical nature of the colloids results in the gradual shrinking of the protected underlying area as the milling progresses. This will result in a different geometry of the created disks, compared to disks created with HCL. More specifically, they can potentially have a different edge slope which may affect the resonance. No matter which nanodisk manufacturing protocol is used, the disks will not be perfect cylinders but will have sloped walls. If there is a large difference in the disk geometry for disks created using HCL or CL, comparisons between the two will be lacking in utility. The extinction spectra in figure 4.11 shows, however, that the resonances are relatively similar, indicating that the disks are approximately equal in shape.

4.2.2 Extinction spectra of Au disks on SOG-coated glass slides

The extinction spectra of similar disks placed on the two different substrates is shown in figure 4.12. As can be seen, there is in this case a spectral shift of about 13 nm which is a large enough difference to potentially affect the biosensing sensitivity. It is worth noting that the resonance peak is broader on SOG than on the glass slides.

4.2.3 CL on waveguides

When CL was used for the deposition of disks on the waveguide chips, the CYTOP surface was seemingly damaged as expected. This did, however, seem to have a rather limited effect on the LSPR excitement. Figure 4.13 shows micrographs of

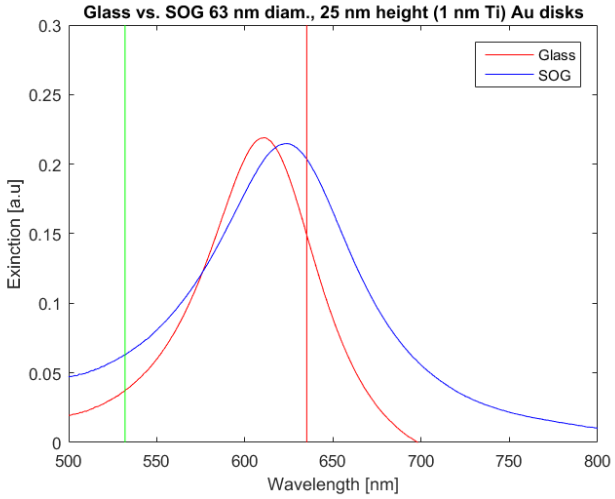

Figure 4.12: Comparison of the spectra for Au disks on a standard and a SOG coated glass slide. There is a 12.8 nm difference in peak position for the two spectra, a large enough difference to affect the tuning of the disk dimensions to the laser wavelength. The red and green vertical lines are the 635 nm and 532 nm wavelength of the lasers used in the binding experiments. The disks were created using 0.1wt% 63 nm colloid solution, with 1 nm Ti and 25 nm Au.

two waveguide surfaces with gold nanodisks prepared by CL and HCL respectively. The images show comparable signal-background ratios but the CL case actually has better uniformity of disk intensity. This may be explained by the fact that the longer and more complex HCL process includes more potential ways of introducing surface contaminations and non-uniformity. This is exemplified in the image as the variation in disks size and the non-circular features apparent on the HCL image.

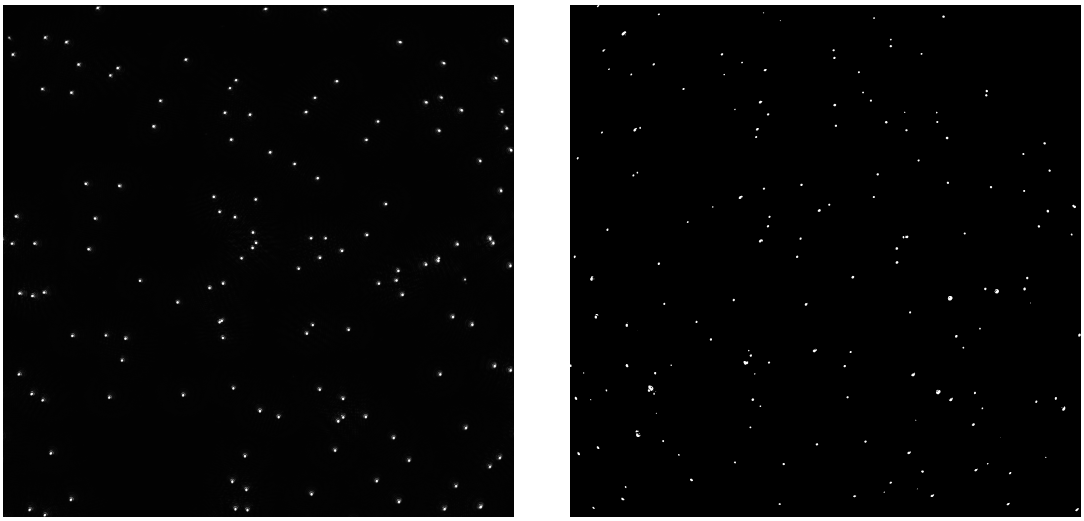

(a) **(b)**

Figure 4.13: Optical micrographs of 100 nm disks excited through waveguide illumination. The disks were deposited through a) CL and b) HCL.

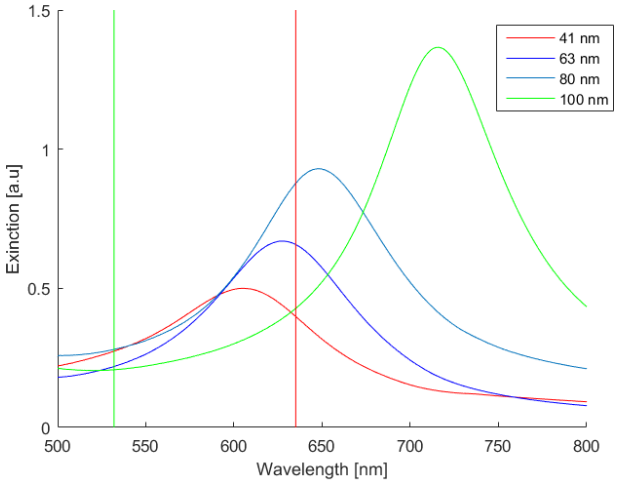

Figure 4.14: Optical extinction spectra of disks with varying diameter (41, 63, 80 and 100 nm) and constant height (1 nm Ti and 25 nm Au) in a water environment. The vertical lines indicates the wavelengths of the lasers used in the vesicle binding experiments, 532 nm and 635 nm.

4.3 Tuning of disk diameter

As mentioned in section 3.1, the setup used for observing the binding of vesicles to nanodisks requires the tuning of the disk LSPR to the specific laser wavelengths. The detection of a vesicle exploits the change of refractive index in the environment near a disk as it displaces water and takes its place. This leads to a shift of the extinction spectrum which is transduced to a detectable shift of scattering intensity. To maximize this intensity shift, and thus maximizing the limit of detection for biosensing applications, the laser illumination wavelength should coincide with the steepest part of the extinction spectrum. The setup has three available laser wavelengths: 488, 532 and 635 nm. The spectra of the disks, decided by the disk dimensions, should thus be tuned to the laser wavelengths. In figure 4.14, the extinction spectra of disks with varying diameter and constant height is shown together with the laser wavelengths for the 532 and 635 nm lasers. The 41 and 63 nm spectra coincides relatively well with both laser wavelengths. A binding induced redshift would thus lead to an intensity increase in the red channel and a decrease on the green channel for these disks. As the disk diameter is increased, the 532 nm laser is located on decreasingly steep parts of the spectra, leading to smaller possible intensity shifts. The larger disks do, however, have steeper slopes, which may compensate for this by a larger intensity shift for the 635 nm laser illumination.

4.4 Spectral shift measurements

To investigate the magnitude of the spectral shift due to changes in the refractive index of the local environment of the gold disks, biological matter in the form of NA or vesicles was added to golddisk coated glass slides as the ensemble spectrum was

measured using the spectrometry setup.

In figure 4.15 a), the spectral centroid position can be seen as a function of time for a glass slide coated with 63 nm diameter gold disks as NeutrAvidin is added. The measurement starts with the sample immersed in water. At $t = 137$ s, the pump is started and begins injecting PBS into the flow cell. At $t = 1065$ s NeutrAvidin solution (200 ug/ml) is injected and at $t = 2365$ s PBS is injected again. Since the refractive index of PBS is close to that of water[56], the blueshift as the PBS is added is likely due to contaminants being rinsed of the sample. As the NA adsorbes to the disks the spectra is red shifted approximately 2.6 nm. A shift of 2.6 nm would correspond to a 3.5 % increase of the red/green signal ratio for a SOG coated glass slide. For a spectrum optimally tuned to the illumination laser wavelengths, this signal ratio increase could at a maximum be approximately 8%.

In figure 4.15 b), the spectral centroid position can be seen as a function of time for a glass slide coated with 63 nm diameter gold disks as POPC vesicles are added. PBS is injected at $t = 280$ s, vesicles at $t = 1850$ s and PBS rinsing is started at $t = 4160$ s. The redshift as the vesicles bind to the surface is 1.5 nm. This is lower value than for the NA as expected since the hollow nature of the vesicles entails a lower refractive index[57]. The slight redshift at the end, during the PBS rinsing, could be due to the reduced scattering of light in the solution as the unbound vesicles are removed.

In figure 4.15 c) the spectral centroid position can be seen as a function of time for a SOG coated glass slide with 63 nm diameter gold disks as POPC vesicles are added. A redshift of approximately 1.5 nm is seen here as well. The spikes in the data are due to air bubbles passing through the system. In contrast to b), the rinsing in this case leads to a blueshift; possibly due to vesicles detaching from the surface. The 1.5 nm shift corresponds to a 1.9% signal ratio shift (3.8% if optimally tuned.) Shifts of 1.5-2.6 nm seems to be in the same order as other studies have reported for avidin-molecules binding to nanoplasmonic structures[1, 13, 58]. A 2.6 nm centroid shift would for a 41 or 100 nm diameter sample, correspond to a 5.9% or 3.2% signal ratio shift, respectively.

4.5 Binding of vesicles

4.5.1 Chip characterisation

In figure 4.16 an example of 100 nm diameter gold nanodisks can be seen as appearing when observed using the optical setup. As can be seen, the disks are seemingly well coupled to the guided light in the SOG core, scattering light with a high intensity and provides a strong contrast to the dark background. Figure 4.17 shows the intensity to background ratio as a function of laser output power for 63 nm disks illuminated with the green and red laser. By optimizing the coupling through the adjustment of the fiber position relative to the chip, it is possible to reach signal background ratios in the hundreds. Looking at figure 4.14 we can see that the red laser is closer to the LSPR peak than the green, which explains the higher ratio for

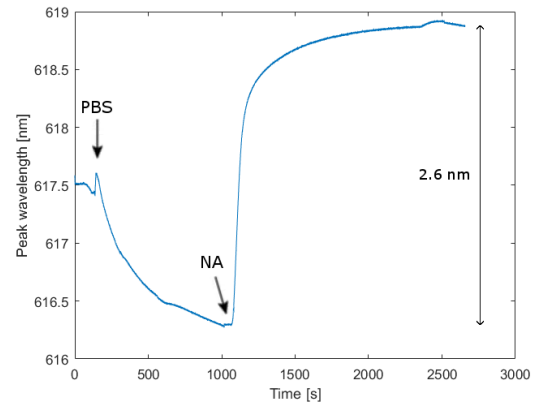

(a)

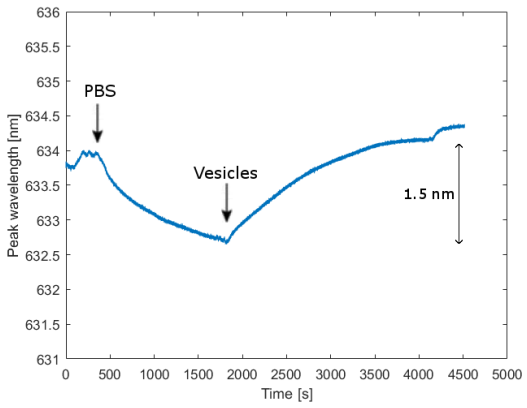

(b)

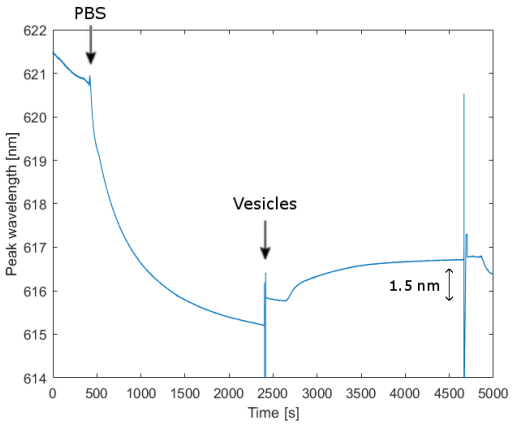

(c)

Figure 4.15: a) LSPR centroid position as a function of time as the sample is immersed sequentially in water, PBS, NA and PBS. The centroid position is redshifted 2.6 nm as the NA is introduced. b) Similar measurement where vesicles are added instead of NA. This gives a centroid shift of approximately 1.5 nm. c) Vesicles added to SOG coated glass slide covered with 63 nm diameter disks.

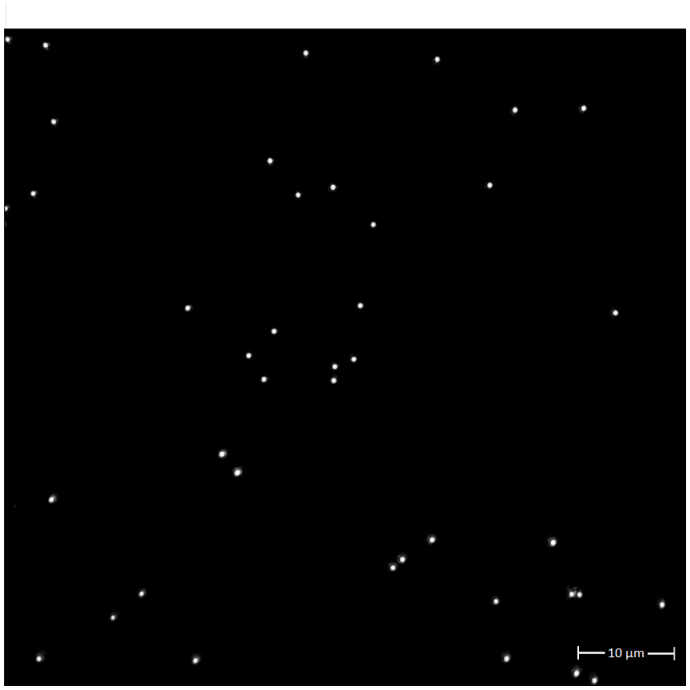

Figure 4.16: Optical image of 100 nm diameter disks consisting of 1 nm Ti and 25 nm Au, illuminated by 635 nm 1750 mV laser light coupled through a waveguide. Note that the bright spots in the image are not the actual disks, as is the case in the SEM images previously shown, but instead laser light scattered from the disks, which themselves have diameters well below the diffraction limit. The spots in the image have approximately the same size as the 635 nm laser wavelength.

figure 4.17 b).

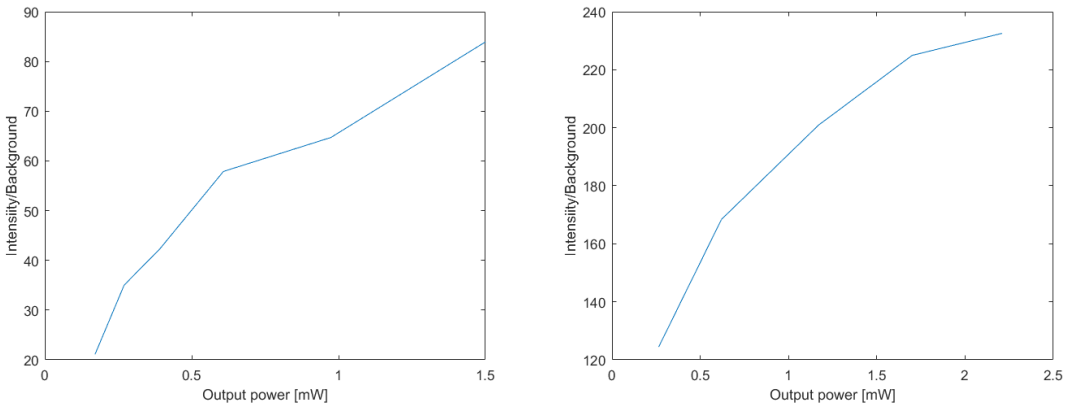

(a) 532 nm **(b)** 635 nm

Figure 4.17: The gold disk intensity divided by the background intensity as a function of the laser power for 63 nm disks deposited on waveguide chips and observed in the optical microscope setup.

For the binding to be detectable, the LSRP frequency shift must induce an intensity

shift larger than the system noise. Figure 4.18 shows the measured intensity, the signal, over time for disks placed in the setup for the green and red lasers. As can be seen, there are some variations in the intensity over time as discussed in section 3.9. The signal to noise ratio, here defined as the mean over the standard deviation of the signal, is measured to 82.92 for the green laser and 66.32 for the red. This does, however, depend on the input power as previously discussed.

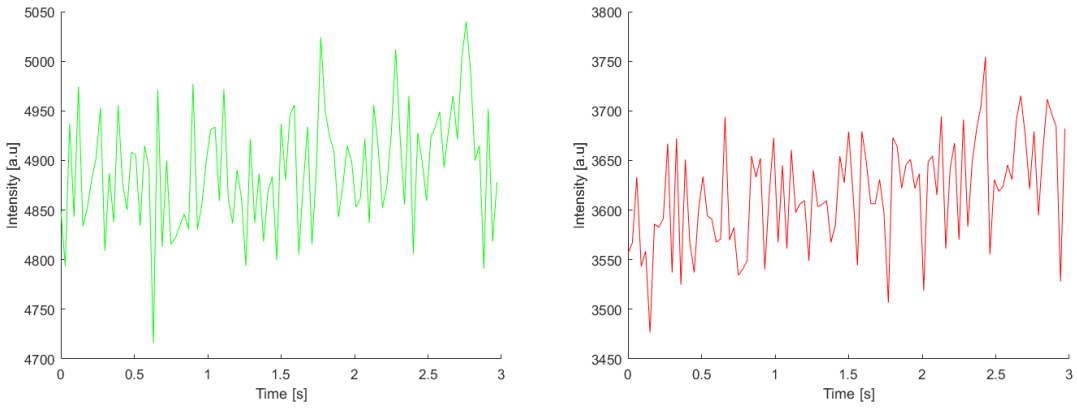

(a) **(b)**

Figure 4.18: The intensity over time for 100 nm diameter gold nanodisks on a waveguide when illuminated with a) 532 nm laser at 2 mW output power and b) 635 nm laser at 2 mW output power.

4.5.2 Binding experiments

To test the potential of using the golddisk coated waveguide chip as a biosensor, the optical microscopy setup described in section 3.8 and the surface chemistry protocol of section 3.5 was used. Briefly, a gold disk coated waveguide chip is functionalized with thiol-PEG-biotin to promote vesicle binding to the gold and PLL-g-PEG to prevent unspecific binding of vesicles to the SOG. The plasma ashing procedure before the incubation did not affect the disk quality in any way visible with the optical microscope setup.

The beam splitter used in the setup makes possible the simultaneous acquisition of two channels. The red emission of rhodamine B labeled vesicles can thus be observed separately from the green excitation signal, which also induces LSPR in the disks.

Figure 4.19 shows an observation of a vesicle binding experiment on a waveguide chip using the optical microscopy beamsplitter setup. The left and right sections of the image shows different parts of the electromagnetic spectrum, above and below 560 nm respectively, for the same area of the waveguide chip well. In this image the sample is illuminated with the 532 nm laser which entails that the left part shows the scattering of the green light on the gold disks and vesicles (the high intensity spots are the nanodisks, observing the sample before vesicle binding enables disk

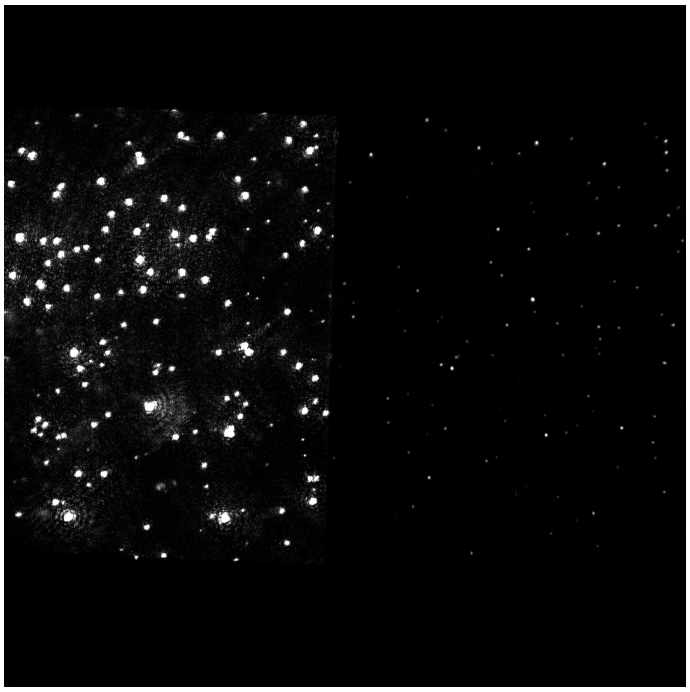

Figure 4.19: Photomicrograph of the waveguide core surface after a binding experiment where rhodamine labeled vesicles are bound to thiol-PEG-biotin on the gold disk surfaces. The image was split by a beamsplitter to show the excitation (left) and emission (right) signals separately.

identification) while the right side shows the red fluorescence emission from the rhodamine molecules on the vesicles. Thus, every spot on the right side corresponds to a vesicle bound specifically to a disk or unspecifically to the SOG surface. Post measurement image analysis can be done by overlaying the two channels (see figure 4.20). A green spot coinciding with a red disk corresponds to a vesicle bound to a disk while other green spots indicate unspecifically bound vesicles.

Figure 4.20 actually shows one of the more successful vesicle binding experiments done during this project, since there is a relatively large number of vesicle bound to gold disks. Getting this level of correlation between bound vesicles and disks proved to be a challenge. Experiments more representative of the majority are shown in figure 4.21. There were either a large quantity of unspecific binding, as in a) or no binding to the disks at all as in b).

To improve the amount of specific binding to the disks, a range of different parameters were varied during the surface functionalization procedure. In the beginning of the project, hydrogen plasma was used to clean and activate the sample surface before the first incubation step. This treatment occasionally produced a relatively high degree of disk-vesicle correlation but did, however, not prove to accomplish this consistently.

After transitioning to an oxygen plasma based surface treatment, moderately more

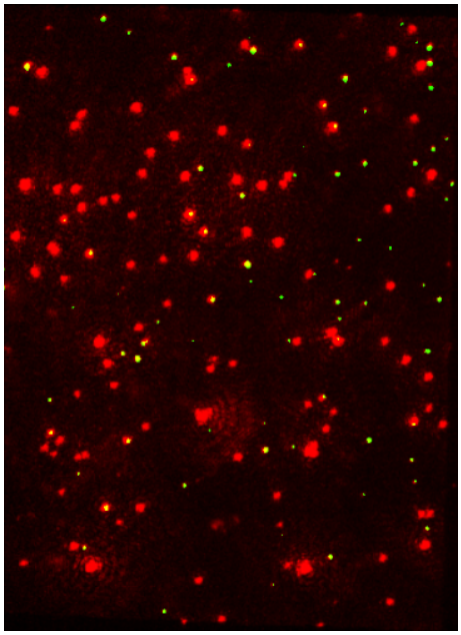

Figure 4.20: The two channels of the image in figure 4.19 shown overlain, where the scattering (primarily from the disks) is red and the fluorescence emission is green. There is some correlation between the disks and vesicles, but there are also unspecifically bound vesicles on the SOG surface.

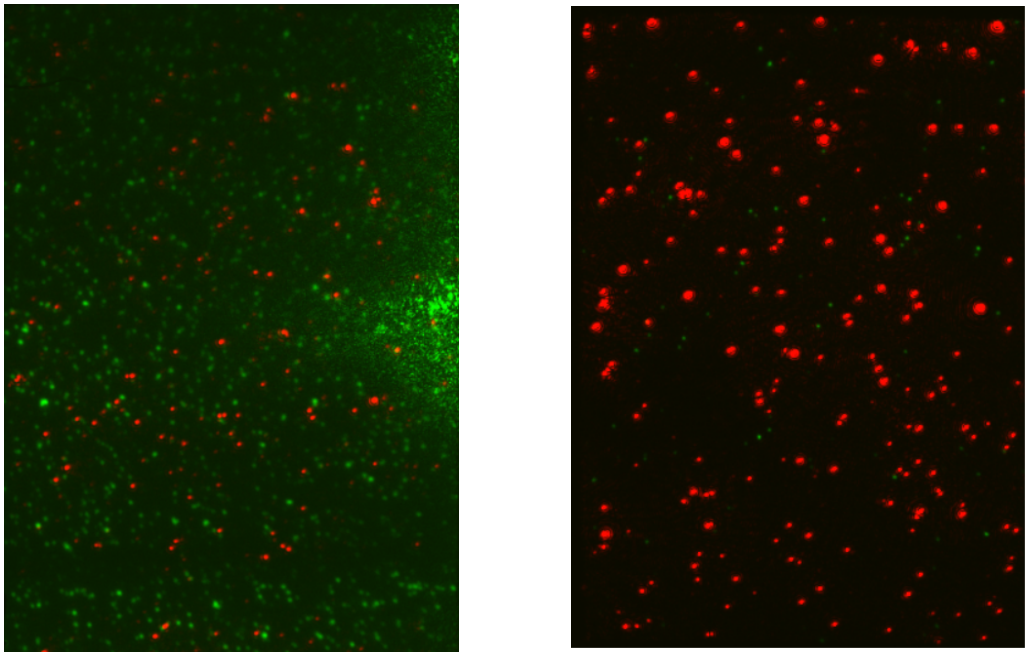

(a) **(b)**

Figure 4.21: Examples of experiments where no vesicles bound to the gold disks. In a), a large amount of unspecific binding can be seen while b) shows relatively little binding in general.

reliable results were achieved. The time of incubation was varied for the different steps. Prematurely terminating the incubation inhibits successful SAM formation, but SAM formation is also dependent on the amount of convection in the incubation solution which was induced through pipette blending to reduce the required incubation time. After incubating a gold surface in thiols, some procedures[49, 51] involve sonicating the sample in ethanol to remove non-covalently bound thiols. This was tried on a number of samples and did increase the correlation rate. Sonicating the waveguide chips in ethanol will, however, quite rapidly cause the detachment of the top CYTOP layer which sets a constraint on this treatment to a maximum of 15 seconds.

A range of different concentrations of biotinylated thiols was used, but for the anti-biotin vesicles, no improvement could be reached by reducing the concentration from 100%.
All binding experiments shown in this section are done using the anti-biotin vesicle procedure. A number of experiments was also done using biotinylated vesicles and an NA-linker (see section 3.5). None of these trials showed any successful binding to the gold disks.

If the binding process works like theoretically intended, no vesicles should be able to bind the the chip except on the gold disks, since all other areas are protected by a layer of the vesicle repelling PEG molecules. Since this was not the case, two hypotheses were considered. Either the PLL-g-PEG SAMs on the SOG is not covering the entire surface, leaving exposed SOG areas, or the biotinylated thiols are binding to something other than the gold, positioning biotin on the SOG. To distinguish between these two ideas, a glass slide surface was functionalized with either sh-PEG-biotin and PLL-g-PEG or just PLL-g-PEG. Micrographs of these two cases after fluorescent vesicles have been added can be seen in figure 4.22 where it is clear that the thiol functionalization significantly increases the unspecific binding even though the thiols are not expected to bind to the glass surface. The unspecific binding is, however, present in both cases, indicating that both hypotheses may be correct.

The unspecific binding to the SOG is less of a problem than the lack of specific binding to the disks. Unspecifically bound vesicles may slightly complicate data analysis and may scatter light which can affect the sensitivity of the measurement but lack of specifically bound vesicles to the gold disks nullifies the possibility of binding detection through refractive index variations completely. The most substantial improvements of the specific binding was the modifications of the plasma treatment and the reduction of the time of sample exposure to the atmosphere between the funcionaliation steps.

For measurements with specific binding, the binding induced refractive index shift could be gauged by observing the intensity shift of the disks. The intensity was recorded over time as vesicles were added to the functionalized chips. The fact that vesicles did not bind to all disks actually brings with it a benefit since dividing

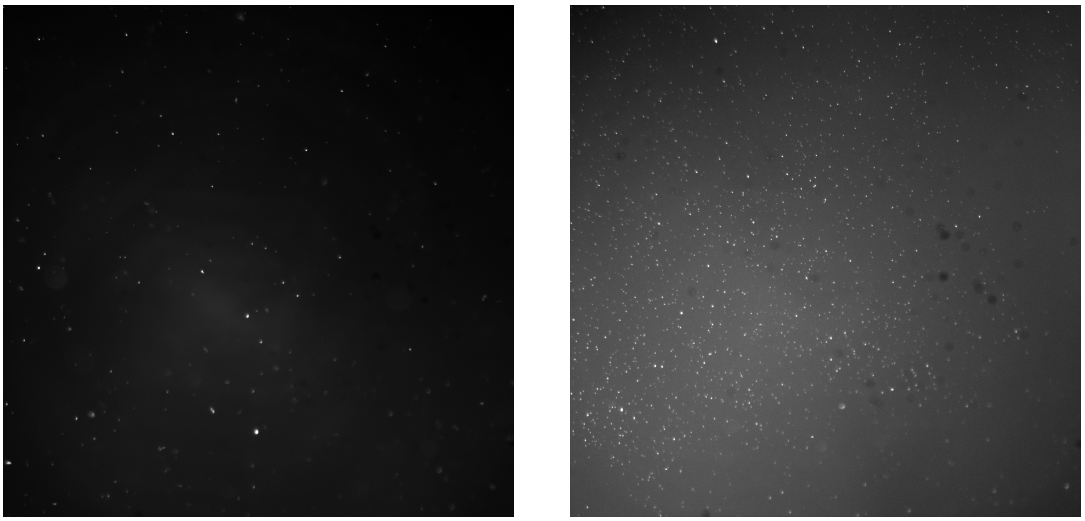

(a) **(b)**

Figure 4.22: Comparison between a glass surface functionalized with both SH-PEG-biotin and PLL-g-PEG or just PLL-g-PEG in an environment containing fluorescent vesicles. The SH-PEG-biotin seems to increase the unspecific binding of vesicles even though no thiol-binding to the glass is expected.

the intensity of a bound disks with an unbound one eliminates intensity changes common for them both. This includes fluctuations in laser intensity, drift of focus and potentially parts of the mechanically induced noise. Figure 4.23 shows the intensity over time for two disks as a vesicle is bound, normalized with an unbound disk. The average intensity increases 2.2 % for a) and 3.0% for b) as the vesicle is bound. A 2.2% increase would correspond to a centroid shift of 2.3 nm which is relatively close to the expected 1.5 nm shift. The SNR for the data is 35.8 and 16.4, which corresponds to noise induced intensity shifts of 6.1% and 2.8% respectively. The expected shift due to binding is up to 3.8% as discussed in section 4.4. Figure 4.24 shows a negative control, where a disk on the same sample without binding was analyzed. This disk shows an 8.1% intensity increase over time as the vesicle solution is added, even if no binding to the disks occurs. This casts doubt on the ability of the system to detect binding events.

In other experiments, NA was added directly to non-functionalized chips. The lack of SAMs makes the NA precipitate closer to the surface than the vesicles would. NA is also more dense and has a higher refractive index[59] and should therefore induce a larger response. Figure 4.25 shows the intensity over time for a chip with 63 nm diameter disks. As discussed in section 4.3, an increase in red and a decrease in green intensity is expected for this disk size. Thus, both channels were used and the intensity of the scattered red light was normalized to the scattered green light. A possible source of error, not present in the vesicle binding measurements, is the fact that all disks are simultaneously covered with NA. It is thus not possible to remove source noise by normalizing the data to an unbound disk. The data was instead normalized to the background, which may account for some of these effects, but not as good as otherwise possible. Focus drift should not be a large issue since it would

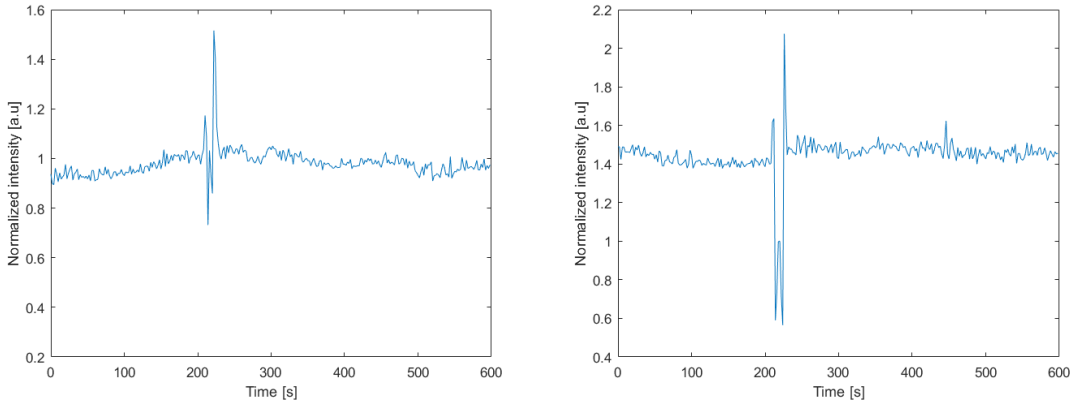

(a) **(b)**

Figure 4.23: Intensity over time for two 63 nm Au disks as vesicles are bound, normalized to disks with no binding. The spikes in the data is the point in time where the vesicle solution is added to the sample.

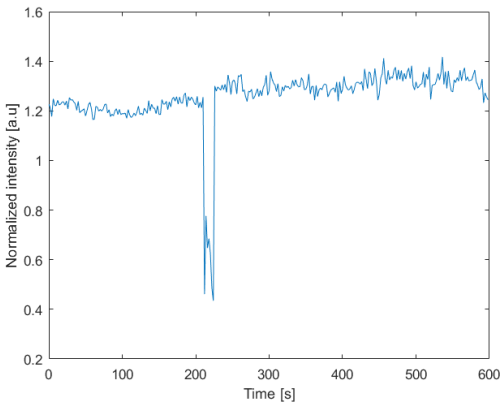

Figure 4.24: The same chip and measurement as in figure 4.23 but showing the intensity over time for a disk where no binding occurs, normalized in the same way as the other plots.

affect the red and green channels in approximately the same way. The increase in intensity for this measurement of 19.7%, a way larger value than expected, does however indicate that there is some relatively large source of intensity shift which is not accounted for. As can be seen in figure 4.25 b), the intensity of the red laser fluctuates considerably more than the green. This is the case in many of the measurements. It is not clear what the source of this noise on the red channel is, but a possible explanation is a temporary increased fluctuation in the source intensity.

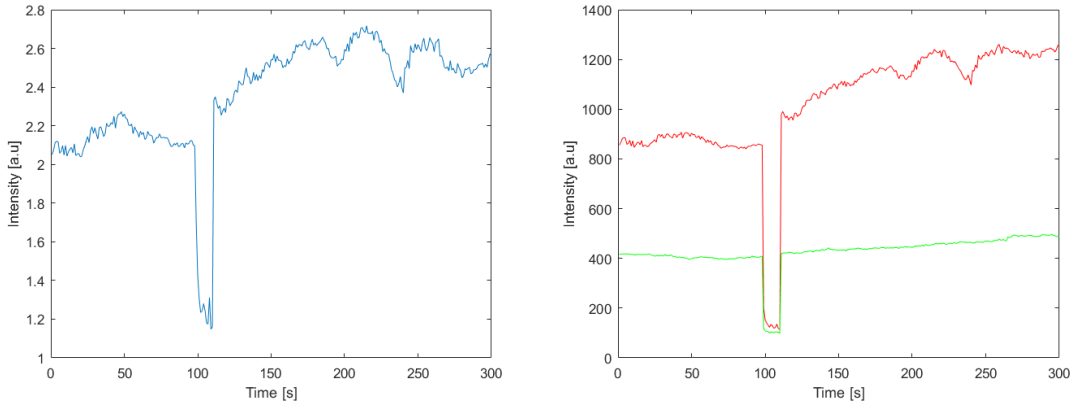

(a) **(b)**

Figure 4.25: Intensity of 63 nm diameter Au nanodisks as NA is added a) Intensity of the red channel over the green. A larger than expected increase is evident. b) The two channel intensities shown separately. The red channel shows high noise and intensity drift levels.

Figure 4.26 shows the intensity over time for a sample with 100 nm disks and as expected, the intensity decreases as the NA is added. b) shows the sample a time after NA have been added, where the solution on the chip is mixed with a pipette. This makes the intensity first increase and then drop, maybe due to NA detaching from the surface and then precipitating again over time. Intensity decrease of 8.7 % in a) and 7.8% in b).

Figure 4.27 shows the intensity over time for a sample with 41 diameter disks as NA is added which gives an intensity increase of 11.1%. This would correspond to a spectral shift of 4.1 nm, instead of the expected 1.5 nm.
The measured intensity shifts in these binding experiments often highly exceeds the expected values based on the observed spectral shifts in the spectroscopic measurements on the glass slide samples. The largest shift observed during the spectral measurements was 2.6 nm which occurred when NA was added to a sample with 63 nm diameter disks. This translates to an approximately 8% intensity shift if the laser wavelength coincides with the maximum derivative of the spectrum slope. As seen above, many of the measured intensity shifts were larger than this and in some cases by multiple times. The data concerning the intensity shift can thus be considered inconclusive. Other sources of intensity shifts are drowning the RI-change induced effects. In the data for the 41 and 63 nm disks, the red channel intensity

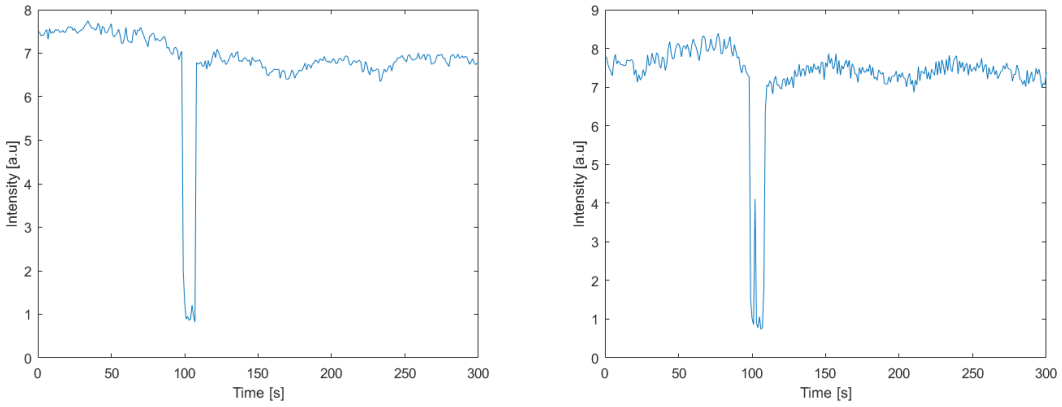

(a) **(b)**

Figure 4.26: Intensity of 100 nm Au disks over time as NA is added. a) shows the time where the NA is added b) shows a later time period, where the solution on the chip is mixed through pipetting.

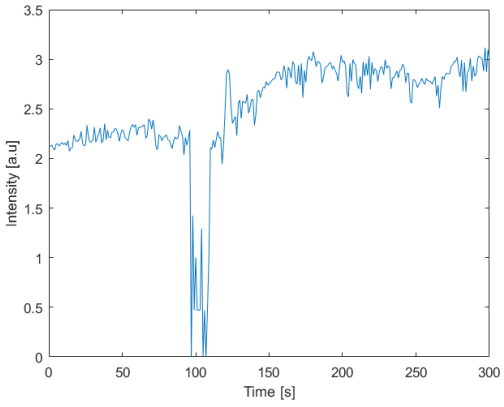

Figure 4.27: Intensity of 41 nm diameter Au nanodisks as NA is added. Intensity of the red channel over the green. A larger than expected increase is evident.

was divided with the green to further visualize the shift and eliminate common drift effects. It is possible that this noise reduction procedure is less efficient than expected. For instance, focus drift could also affect the channels differently if they are not equally intense, something that is not easily controlled during the experiment; where intensity distributions between individual disks, saturation level and laser input intensity fluctuations have to be considered on the fly. It is also possible that as the NA or vesicles are pipetted to the chip, the system is mechanically disturbed and unintentionally set slightly into motion. This could affect the laser coupling to the chip, which may unequally affect the different laser wavelengths. In any case, the expected intensity shifts are of the same magnitude as the system inherent noise levels. This means that even without possible external disturbances, the shift, while possible through considering average intensity differences, would be difficult to observe.

An alternative approach to these kinds of measurements would be to spectroscopically analyze the individual disks as biological matter are bound to them. This would require a different setup where the 100x magnification optics are combined with some type of spectrally sensitive equipment, tentatively a liquid crystal tunable filter placed in front of the CCD camera in the setup. This would allow for the acquisition of spectra for each individual disk and eliminate the need of tracking intensity shifts at discrete wavelengths as done in the test in this project. Intensity fluctuations would thus be distinguishable from LSPR spectral shifts. The major drawback of this method is that since a spectroscopic analysis requires a continuum of wavelengths, a white light source coupled to the waveguide is needed instead of the single wavelength lasers used here. Intensity stable and continuous white laser sources exists[60], but are expensive.

If the transition to white laser illumination is not possible, other approaches to increase the intensity shifts could be employed. It could for example be accomplished by using nanostructures with sharper LSPR peaks. This would make a spectral shift give a larger intensity response compared to using circular nanodisks as in this project. Investigations of how to optimize the shape and features of HCL-compatible nanostructures for this purpose have been done[26, 27].

The surface chemistry problems concerning the lack of binding to the gold disks could potentially be improved by a different cleaning procedure before initiating the surface functionalization. Many use TL1 (5:1:1 water: 30% H_2O_2 : 30% NH_4OH) [61], RCA1 (5:1:1 water: 30% H_2O_2 : 30% NH_3) [11] or similar procedures. Using these on the waveguide system do, however, risk destroying it through interactions with the CYTOP, SOG and Ti layers. Investigating if these methods could be adapted the be used on the waveguides may provide a way of improving the SAM formation on and binding to the gold disks.

5

Conclusion and outlook

In conclusion, protocols for the integration of gold nanodisks on the waveguide using HCL or CL have been successfully developed. The less complex CL method gives a higher disk homogeneity but will inevitably etch the waveguide surface between the produced disks. This may cause problems regarding the specific binding of analytes to the disk surfaces. The HCL method is less harmful to the SOG surface quality but gives a somewhat less homogeneous disk size distribution. The disks shows a high signal-background ratio and could potentially be used for sensitive refractive index measurements by observing LSPR shifts.

The used proof-of-concept setup proved to be very sensitive to external sources of noise and drifts of intensity, especially when using the 635 nm laser for LSPR excitation.

An alternative approach which would likely eliminate many of the problems concerning the limited sensitivity is to analyze the spectra of individual disks on the waveguide surface. This would allow for the tracking of shifts in the LSPR spectral centroid position but would require the transition to a white supercontinuum laser source[60]. An intensity stable and continuous source would allow for spectroscopic analysis of single nanodisks on the waveguide surface.

An increase in the system sensitivity could also be accomplished by optimizing the nanostructure shape and material to maximize the LSPR peak shift due to RI variations. Nanorings and nanocresents are examples of colloidal lithography-compatible structures shown to produce increased sensitivity[27].

The waveguide chips without any plasmonic structures has previously been used for biosensing experiments[9]. In these cases, analytes are observed through their scattering of the evanescent light as they bind to the surface with no LSPR spectra involved. It is thus possible to see scattering from individual particles in the 100 nm range using this system. In the experiments in this thesis, the scattering signal from a vesicle bound to a gold disk is drowned in the disk scattering intensity. This is not a problem since it is the effect a vesicle has on the disk scattering that is the experiment observable. If achieving a high sensitivity for this approach, the smaller size ranges of vesicles, not accessible by the sole observation of their own scattering, could be observed; but for larger analytes, the nanodisk approach may be unnecessary.

The process of using this system for biosensing would be significantly more convenient if a reliable surface chemistry protocol is available. More specifically, being able to consistently specifically bind analytes to the disks. The experiences gained during this project points at an investigation of the pre-functionalization cleaning procedure as a reasonable starting point for optimizing this.

An interesting method to optimize the thickness of the different material layers in the system would be to use a partially exposed rotating substrate during the PVD steps in the manufacturing[62]. A single substrate could then exhibit a continuum of disk thickness. This could also be used for varying the waveguide core thickness which would give a gradually increasing evanescent field penetration depth.

Bibliography

[1] A. Dahlin, *Plasmonic biosensors: An integrated view of refractometric detection*. IOS Press, 2012.

[2] A. Dmitriev, *Nanoplasmonic Sensors*. Springer US, 2012.

[3] E. Cocucci and J. Meldolesi, "Ectosomes and exosomes: shedding the confusion between extracellular vesicles.," *Trends in cell biology*, vol. 25, pp. 364–72, jun 2015.

[4] M. P. Caby, D. Lankar, C. Vincendeau-Scherrer, G. Raposo, and C. Bonnerot, "Exosomal-like vesicles are present in human blood plasma," *International Immunology*, vol. 17, pp. 879–887, may 2005.

[5] V. Palanisamy and S. et. al, "Nanostructural and Transcriptomic Analyses of Human Saliva Derived Exosomes," *PLoS ONE*, vol. 5, p. e8577, jan 2010.

[6] T. Pisitkun, R.-F. Shen, and M. A. Knepper, "Identification and proteomic profiling of exosomes in human urine.," *Proceedings of the National Academy of Sciences of the United States of America*, vol. 101, pp. 13368–73, sep 2004.

[7] P. Joshi, L. Benussi, R. Furlan, R. Ghidoni, and C. Verderio, "Extracellular Vesicles in Alzheimer's Disease: Friends or Foes? Focus on Aβ-Vesicle Interaction," *International Journal of Molecular Sciences*, vol. 16, pp. 4800–4813, mar 2015.

[8] A. Mehdiani, A. Maier, A. Pinto, M. Barth, P. Akhyari, and A. Lichtenberg, "An innovative method for exosome quantification and size measurement.," *Journal of visualized experiments : JoVE*, p. 50974, jan 2015.

[9] B. Agnarsson, A. Lundgren, A. Gunnarsson, M. Rabe, A. Kunze, M. Mapar, L. Simonsson, M. Bally, V. P. Zhdanov, and F. Höök, "Evanescent Light-Scattering Microscopy for Label-Free Interfacial Imaging: From Single Sub-100 nm Vesicles to Live Cells," *ACS Nano*, vol. 9, no. 12, pp. 11849–11862, 2015.

[10] A. V. Vlassov, S. Magdaleno, R. Setterquist, and R. Conrad, "Exosomes: Current knowledge of their composition, biological functions, and diagnostic and therapeutic potentials," *Biochimica et Biophysica Acta (BBA) - General Subjects*, vol. 1820, pp. 940–948, jul 2012.

[11] A. B. Dahlin, J. O. Tegenfeldt, and F. Höök, "Improving the Instrumental Resolution of Sensors Based on Localized Surface Plasmon Resonance," *Anal. Chem.*, vol. 78, no. 13, pp. 4416–4423, 2006.

[12] Z. Liu and P. C. Searson, "Single nanoporous gold nanowire sensors," *The Journal of Physical Chemistry B*, vol. 110, no. 9, pp. 4318–4322, 2006.

[13] Greg J. Nusz, Stella M. Marinakos, Adam C. Curry, Andreas Dahlin, Fredrik Höök, Adam Wax, and Ashutosh Chilkoti, "Label-Free Plasmonic Detection of Biomolecular Binding by a Single Gold Nanorod," *Analytical Chemistry*, 2008.

[14] M. Faraday, "The Bakerian Lecture: Experimental Relations of Gold (and Other Metals) to Light," *Philosophical Transactions of the Royal Society of London*, vol. 147, pp. 145–181, jan 1857.

[15] G. Mie, "Beiträge zur Optik trüber Medien, speziell kolloidaler Metallösungen," *Annalen der Physik*, vol. 330, no. 3, pp. 377–445, 1908.

[16] M. I. Stockman, "Nanoplasmonics: past, present, and glimpse into future," *Optics express*, vol. 19, no. 22, pp. 22029–22106, 2011.

[17] E. M. Larsson, C. Langhammer, I. Zorić, and B. Kasemo, "Nanoplasmonic probes of catalytic reactions," *Science*, vol. 326, no. 5956, pp. 1091–1094, 2009.

[18] S. A. Maier, *Plasmonics: Fundamentals and Applications*. Springer US, 2007.

[19] U. Kreibig and M. Vollmer, *Optical Properties of Metal Clusters*. Springer Series in Materials Science, Springer Berlin Heidelberg, 2013.

[20] F. Wooten, *Optical Properties of Solids*. Elsevier Science, 1972.

[21] P. Drude, "Zur Elektronentheorie der Metalle," *Annalen der Physik*, vol. 306, no. 3, pp. 566–613, 1900.

[22] J. Ortega-Mendoza, A. Padilla-Vivanco, C. Toxqui-Quitl, P. Zaca-Morán, D. Villegas-Hernández, and F. Chávez, "Optical Fiber Sensor Based on Localized Surface Plasmon Resonance Using Silver Nanoparticles Photodeposited on the Optical Fiber End," *Sensors*, vol. 14, no. 10, pp. 18701–18710, 2014.

[23] A. J. Haes, S. Zou, G. C. Schatz, and R. P. Van Duyne, "A nanoscale optical biosensor: the long range distance dependence of the localized surface plasmon resonance of noble metal nanoparticles," *The Journal of Physical Chemistry B*, vol. 108, no. 1, pp. 109–116, 2004.

[24] N. Nath and A. Chilkoti, "Label-free biosensing by surface plasmon resonance of nanoparticles on glass: Optimization of nanoparticle size," *Analytical Chemistry*, vol. 76, no. 18, pp. 5370–5378, 2004.

[25] P. Hanarp, M. Käll, and D. S. Sutherland, "Optical Properties of Short Range Ordered Arrays of Nanometer Gold Disks Prepared by Colloidal Lithography," *The Journal of Physical Chemistry B*, vol. 107, pp. 5768–5772, jun 2003.

[26] K.-S. Lee and M. A. El-Sayed, "Gold and silver nanoparticles in sensing and imaging: sensitivity of plasmon response to size, shape, and metal composition.," *The Journal of Physical Chemistry. B*, vol. 110, pp. 19220–5, oct 2006.

[27] T. Chung, S.-Y. Lee, E. Y. Song, H. Chun, and B. Lee, "Plasmonic nanostructures for nano-scale bio-sensing," *Sensors*, vol. 11, no. 11, pp. 10907–10929, 2011.

[28] I. Zoric, M. Zaäch, B. Kasemo, and C. Langhammer, "Gold, platinum, and aluminum nanodisk plasmons: material independence, subradiance, and damping mechanisms," *ACS nano*, vol. 5, no. 4, pp. 2535–2546, 2011.

[29] N. Félidj, J. Aubard, G. Lévi, J. Krenn, G. Schider, a. Leitner, and F. Aussenegg, "Enhanced substrate-induced coupling in two-dimensional gold nanoparticle arrays," *Physical Review B*, vol. 66, no. 24, pp. 1–7, 2002.

[30] E. Hecht, *Optics*. Pearson education, Addison-Wesley, 2002.

[31] D. Axelrod, "Cell-substrate contacts illuminated by total internal reflection fluorescence.," *The Journal of Cell Biology*, vol. 89, pp. 141–5, apr 1981.

[32] R. Jaeger, *Introduction to Microelectronic Fabrication*. Modular series on solid state devices, Prentice Hall, 2002.

[33] M. Ohring, *The Materials Science of Thin Films*. Referex Engineering, Academic Press, 1992.

[34] A. Broers, A. Hoole, and J. Ryan, "Electron beam lithography - Resolution limits," *Microelectronic Engineering*, vol. 32, no. 1, pp. 131–142, 1996.

[35] D. Ensminger and F. Stulen, *Ultrasonics: Data, Equations and Their Practical Uses*. CRC Press, 2008.

[36] R. d'Agostino, D. Flamm, and O. Auciello, *Plasma Deposition, Treatment, and Etching of Polymers: The Treatment and Etching of Polymers*. Plasma-Materials Interactions, Elsevier Science, 2012.

[37] P. Hanarp, D. S. Sutherland, J. Gold, and B. Kasemo, "Control of nanoparticle film structure for colloidal lithography," *Colloids and Surfaces A: Physicochemical and Engineering Aspects*, vol. 214, no. 1-3, pp. 23–36, 2003.

[38] H. Fredriksson, Y. Alaverdyan, A. Dmitriev, C. Langhammer, D. Sutherland, M. Zäch, and B. Kasemo, "Hole–Mask Colloidal Lithography," *Advanced Materials*, vol. 19, pp. 4297–4302, dec 2007.

[39] Y.-C. Chang, H.-C. Chung, S.-C. Lu, and T.-F. Guo, "A large-scale sub-100 nm Au nanodisk array fabricated using nanospherical-lens lithography: a low-cost localized surface plasmon resonance sensor," *Nanotechnology*, vol. 24, no. 9, p. 095302, 2013.

[40] Z. Adamczyk, M. Zembala, B. Siwek, and P. Warszyński, "Structure and ordering in localized adsorption of particles," *Journal of Colloid and Interface Science*, vol. 140, no. 1, pp. 123–137, 1990.

[41] M. Hope, M. Bally, G. Webb, and P. Cullis, "Production of large unilamellar vesicles by a rapid extrusion procedure. Characterization of size distribution, trapped volume and ability to maintain a membrane potential," *Biochimica et Biophysica Acta (BBA)-Biomembranes*, vol. 812, no. 1, pp. 55–65, 1985.

[42] J. C. Love, L. A. Estroff, J. K. Kriebel, R. G. Nuzzo, and G. M. Whitesides, "Self-assembled monolayers of thiolates on metals as a form of nanotechnology," *Chemical Reviews*, vol. 105, no. 4, pp. 1103–1170, 2005.

[43] A. Ulman, "Formation and structure of self-assembled monolayers," *Chemical reviews*, vol. 96, no. 4, pp. 1533–1554, 1996.

[44] N. Green, "Avidin. 1. the use of [14c] biotin for kinetic studies and for assay," *Biochemical Journal*, vol. 89, no. 3, p. 585, 1963.

[45] C. D. Bain, E. B. Troughton, Y. T. Tao, J. Evall, G. M. Whitesides, and R. G. Nuzzo, "Formation of monolayer films by the spontaneous assembly of organic thiols from solution onto gold," *Journal of the American Chemical Society*, vol. 111, no. 1, pp. 321–335, 1989.

[46] R. Marie, J. P. Beech, J. Vörös, J. O. Tegenfeldt, and F. Höök, "Use of pll-g-peg in micro-fluidic devices for localizing selective and specific protein binding," *Langmuir*, vol. 22, no. 24, pp. 10103–10108, 2006.

[47] M. Heuberger, T. Drobek, and N. D. Spencer, "Interaction forces and morphology of a protein-resistant poly(ethylene glycol) layer.," *Biophysical Journal*, vol. 88, no. 1, pp. 495–504, 2005.

[48] K. Feldman, G. Hähner, N. Spencer, P. Harder, and M. Grunze, "Probing resistance to protein adsorption of oligo (ethylene glycol)-terminated self-assembled

monolayers by scanning force microscopy," *Journal of the American Chemical Society*, vol. 121, no. 43, pp. 10134–10141, 1999.

[49] R. Marie, A. B. Dahlin, J. O. Tegenfeldt, and F. Höök, "Generic surface modification strategy for sensing applications based on AuSiO2 nanostructures.," *Biointerphases*, vol. 2, no. 1, pp. 49–55, 2007.

[50] A. Patra, *Quantifying Interactions of Biomolecules with Inorganic Surfaces*. Springer Theses, Springer International Publishing, 2017.

[51] D. L. M. Rupert, G. V. Shelke, G. Emilsson, V. Claudio, S. Block, C. Lässer, A. Dahlin, J. O. Lötvall, M. Bally, V. P. Zhdanov, and F. Höök, "Dual-Wavelength Surface Plasmon Resonance for Determining the Size and Concentration of Sub-Populations of Extracellular Vesicles," *Analytical Chemistry*, vol. 88, pp. 9980–9988, oct 2016.

[52] J. Goldstein, D. Newbury, D. Joy, C. Lyman, P. Echlin, E. Lifshin, L. Sawyer, and J. Michael, *Scanning Electron Microscopy and X-ray Microanalysis: Third Edition*. Springer US, 2012.

[53] MicroChem, *NANO PMMA and Copolymer*, 2001.

[54] AGC Chemicals, *Amorphous fluoropolymer CYTOP*, 9 2009.

[55] W. Kern, "The Evolution of Silicon Wafer Cleaning Technology," *Journal of The Electrochemical Society*, vol. 137, no. 6, p. 1887, 1990.

[56] L. Diéguez, N. Darwish, M. Mir, E. Martínez, M. Moreno, and J. Samitier, "Effect of the Refractive Index of Buffer Solutions in Evanescent Optical Biosensors," *Sensor Letters*, vol. 7, pp. 851–855, oct 2009.

[57] K. Matsuzaki, O. Murase, K. Sugishita, S. Yoneyama, K. Akada, M. Ueha, A. Nakamura, and S. Kobayashi, "Optical characterization of liposomes by right angle light scattering and turbidity measurement," *Biochimica et Biophysica Acta (BBA)-Biomembranes*, vol. 1467, no. 1, pp. 219–226, 2000.

[58] G. J. Nusz, A. C. Curry, S. M. Marinakos, A. Wax, and A. Chilkoti, "Rational Selection of Gold Nanorod Geometry for Label-Free Plasmonic Biosensors," *ACS Nano*, vol. 3, pp. 795–806, apr 2009.

[59] M. P. Jonsson, P. Jönsson, and H. Fredrik, "Simultaneous nanoplasmonic and quartz crystal microbalance sensing: analysis of biomolecular conformational changes and quantification of the bound molecular mass," *Analytical chemistry*, vol. 80, no. 21, pp. 7988–7995, 2008.

[60] R. Alfano, *The Supercontinuum Laser Source: The Ultimate White Light*. Springer New York, 2016.

[61] S. Chen, M. Svedendahl, M. Käll, L. Gunnarsson, and A. Dmitriev, "Ultrahigh sensitivity made simple: nanoplasmonic label-free biosensing with an extremely low limit-of-detection for bacterial and cancer diagnostics," *Nanotechnology*, vol. 20, no. 43, p. 434015, 2009.

[62] R. Ogier, L. Shao, M. Svedendahl, and M. Käll, "Continuous-gradient plasmonic nanostructures fabricated by evaporation on a partially exposed rotating substrate," *Advanced Materials*, vol. 28, no. 23, pp. 4658–4664, 2016.